https://ntrs.nasa.gov/search.jsp?R=19960020956 2017-08-16T03:57:19+00:00Z

NASA-CR-200839

ELECTROMAGNETIC COMPATIBILITY TESTING STUDIES

Final Technical Report on Grant NAG-1-1510
(6-1-93 to 8-31-95)

To

NASA Langley Research Center
Hampton, Virginia 23681

By

Thomas F. Trost and Atindra K. Mitra

Department of Electrical Engineering
Texas Tech University
Lubbock, Texas 79409

January 15, 1996

ABSTRACT

This report discusses the following results from a study of microwave reverberation chambers performed at Texas Tech University:

Analytical Models

• Two analytical models of power transfer vs. frequency in a chamber, one for antenna-to-antenna transfer and the other for antenna to D-dot sensor.

• Experimental validation of the models in our chamber.

• Two examples of the measurement and calculation of chamber Q, one for each of the models.

Measurement and Simulation of Statistical Properties

• Measurements of EM power density which validate a theoretical probability distribution [7] on and away from the chamber walls and which also yield a distribution with larger standard deviation at frequencies below the range of validity of the theory.

• Measurements of EM power density at pairs of points which validate a theoretical spatial correlation function [7] on the chamber walls and which also yield a correlation function with larger correlation length, R_{corr}, at frequencies below the range of validity of the theory.

• A numerical simulation, employing a rectangular cavity with a moving wall, which shows agreement with the measurements.

• The determination that the lowest frequency at which the theoretical spatial correlation function is valid in our chamber is considerably higher than the lowest frequency recommended by current guidelines for utilizing reverberation chambers in EMC testing.

Suggestions

• Two suggestions for future studies related to EMC testing.

I. INTRODUCTION

The research described in this report has been carried out in support of the activities involving the new microwave reverberation chambers in the HIRF laboratory at the Langley Research Center. The NASA Technical Officers for this research were Felix Pitts and, later, Charles Meissner.

Microwave reverberation (or mode-stirred) chambers were first investigated in Italy by Paolo Corona [1], and the chamber that Corona constructed has just celebrated its twentieth birthday. Although several chambers around the world have been put to use over the years, mainly for the EMC testing of a variety of electronic devices, there has been little rigorous modeling of the electromagnetic environment inside the chambers and around the devices under test. Thus our understanding of the chambers' strengths and weaknesses for EMC applications remains incomplete. The research reported here, which focuses on characterizing chamber fields, is intended as a step toward a fuller understanding.

II. CHAMBER POWER TRANSFER

In an experimental reverberation chamber study [2] carried out at NIST, Crawford and Koepke measured, among other things, the attenuation of a signal sent between two antennas located inside the chamber. They showed that the attenuation (averaged over many paddle wheel positions) increases with frequency, f, at a rate of 25 dB per decade, that is, like

f to the power 2.5, over a certain range of frequencies. They did not say why this occurs. With Crawford and Koepke's paper as a starting point and using some results from Loughry [3] and Dunn [4], we have derived a mathematical model which explains the observed 2.5 power law; and we have also obtained a model, which gives a -1.5 power law dependence for the attenuation, for the case where the receiving antenna in the chamber is replaced by a receiving D-dot sensor. D-dot (and B-dot) sensors [5] were originally developed to measure EMP fields, but they are also useful as field probes inside reverberation chambers because they are small in size and they drain little power from the chamber. As part of our investigation of chamber attenuation we also built our own small chamber (1.034 x 0.809 x 0.581 m) and carried out a series of measurements, which showed reasonable agreement with the 2.5-power and -1.5-power frequency dependencies. A complete discussion of this work is contained in a short paper [6], "Power Transfer Characteristics of a Microwave Reverberation Chamber," which we have submitted for publication and is included as an appendix to this report.

Our two models yield the following equations: For the case of a receiving antenna in the chamber, which we call configuration 1, the power gain is given by

$$G_{ant} = 1/(1 + K_1 f^{2.5}) \qquad (1)$$

and for the case of a receiving D-dot sensor, configuration 2, the gain is

$$G_{\dot{D}} = 1/(1 + K_2 f^{-1.5}). \qquad (2)$$

Expressions for the constants K_1 and K_2 are given in our paper. It can be seen from the first equation that if the frequency, f, is *large* enough, then the second term in the denominator will dominate, so that the gain will vary as $f^{-2.5}$ and thus the attenuation will go as $f^{2.5}$-- Crawford and Koepke's result. On the other hand, if f is *small* enough in the second equation, the gain will go like $f^{1.5}$ and the attenuation like $f^{-1.5}$, as stated in the preceding paragraph.

Our derivation shows that physically what is happening is as follows: In configuration 1 the $f^{2.5}$ attenuation arises from an $f^{2.0}$ factor contributed by the receiving antenna and an $f^{0.5}$ from the chamber walls. The receiving antenna is assumed to have an average gain of 1.0 at all frequencies within its bandwidth, because of the many reflections from the chamber walls; thus its effective area, and the power it extracts from the chamber, decrease with frequency like $f^{2.0}$. The skin depth of the chamber walls decreases with frequency, so that the resistance of the walls and the ohmic losses increase as $f^{0.5}$. In configuration 2 the $f^{-1.5}$ attenuation is due to $f^{-2.0}$ from the D-dot sensor and $f^{0.5}$ from the walls. The sensor output voltage varies linearly with frequency since it is a time-derivative type sensor; thus its output power goes like $f^{2.0}$-- an attenuation of $f^{-2.0}$. The power losses to the chamber walls operate as in configuration 1 to provide the same $f^{0.5}$ effect.

These equations for the gain describe a very general property of reverberation chambers (treated as two-ports). What application do they have to EMC testing? If a chamber is to be used to test the immunity of some electronic device, the device would be placed inside, RF power would be applied to the transmitting antenna, and the receiving antenna/sensor would be used to monitor the field strength. In this situation the value of the gain from the equations above would be of interest because one would want to be sure of having a sufficiently *low* gain, i.e., most of the power staying in the chamber, producing a strong, high-Q field.

III. CHAMBER Q

We determine the Q (or quality factor) of our reverberation chamber using the following equations, which result from simple manipulations of the equations contained in our paper [6]. Note that there are four different Qs given here, all labelled Q_{net}-- the experimental and theoretical for configuration 1 and the experimental and theoretical for configuration 2. Obtaining values for the experimental Qs requires the measurement of the chamber two-port scattering parameters S_{12} and S_{11}, as discussed in our paper [6].

1. Chamber with transmitting antenna and receiving antenna (configuration 1):

(a) Experimental

The Q is given by

$$Q_{net} = G_{ant} Q_{ant} \tag{3}$$

where

$$G_{ant} = |S_{21}|^2/(1 - |S_{11}|^2)$$

with S_{21} and S_{11} measured, and

$$Q_{ant} = 2(\omega/c)^3 V/\pi.$$

(b) Theoretical

The Q is given by

$$Q_{net} = (1/Q_{ant} + 1/Q_{eqv})^{-1} \tag{4}$$

where $Q_{eqv} = 1.5V/(\mu_r S\delta)$.

2. Chamber with transmitting antenna and receiving D-dot sensor (configuration 2):

(a) Experimental

The Q is given by

$$Q_{net} = G_{\dot{D}}\, Q_{\dot{D}} \tag{5}$$

where

$$G_{\dot{D}} = |S_{21}|^2/(1 - |S_{11}|^2)$$

with S_{21} and S_{11} measured, and

$$Q_{\dot{D}} = 1.5V/(RA^2\varepsilon_0\omega).$$

(b) Theoretical

The Q is given by

$$Q_{net} = (1/Q_{\dot{D}} + 1/Q_{eqv})^{-1} \tag{6}$$

where

$$Q_{eqv} = 1.5V/(\mu_r S\delta).$$

In these equations $\omega = 2\pi f$, c = speed of light, V = volume of chamber (0.486 m^3), μ_r = relative permeability of chamber walls (1.0), S = surface area of chamber walls (3.81 m^2), δ = skin depth of chamber walls, R = load resistance of D-dot sensor (50 Ω), A = area of D-dot sensor (1.0×10^{-4} m^2), and ε_0 = permittivity of free space.

In Figs. 1 and 2 we show plots of the Qs obtained from the above equations for our chamber over the frequency range from 1.0 GHz to 10.0 GHz. Fig. 1 gives the results for configuration 1 and Fig. 2 for configuration 2. For both configurations the theoretical Q is about seven times larger than the experimental Q; and so to fit both on the same plot, we have divided the theoretical by a factor of seven. A tendency for this kind of discrepancy between theoretical and experimental Qs in reverberation chambers has been reported by

other workers [3]; the reason for it is not clear. We are currently investigating an alternative method for measuring Q via the chamber impulse response, and so we eventually may be able to shed some light on this discrepancy.

Q is a fundamental parameter of a chamber, and, from it, another important parameter, M, can be obtained, as shown in Eq. 8 in the next section of this report. The graphs of Q versus frequency for our chamber should be useful as a point of comparison with other chambers, such as those at the Langley Research Center.

IV. CHAMBER PROBABILITY DENSITY FUNCTION

In the previous sections of this report dealing with power transfer and Q, we have made use of the average field in a chamber, the result of averaging over many paddle wheel positions. If we look instead at the results for all the positions, then we get a distribution of values; and the form of this distribution is of vital interest if the chamber is to be used in any EMC-testing applications.

A statistical theory has been developed by Ted Lehman [7] for the fields inside of what Lehman refers to as a "complex cavity." In order to see to what extent this theory predicts the behavior of the fields in our reverberation chamber-- to answer the classic scientific question: is the theory validated by experiment?-- we have carried out a comparison of probability density functions (PDFs) and spatial correlation functions (SCFs), Lehman's theoretical functions versus our measured functions. In what follows, **E** is electric field, E_i is one vector component of **E**, and Z_0 is the intrinsic impedance of free space.

For each vector component of the EM power density, $P_i = |E_i|^2/Z_0$, in his complex cavity, Lehman found an exponential distribution described by the following PDF:

$$f(P_i) = (1/P_0)\exp(-P_i/P_0)$$

where P_0 is the mean of P_i. When P_i is expressed in dB as $P_{idB} = 10\log(P_i)$, an extreme value distribution is obtained:

$$f(P_{idB}) = (1/\beta)\exp[(1/\beta)(P_{idB} - P_{0dB}) - \exp[(1/\beta)(P_{idB} - P_{0dB})] \qquad (7)$$

where $\beta = 4.3429$ and $P_{0dB} = 10\log(P_0)$. The standard deviation, σ, for $f(P_{idB})$ is 5.57 dB. To obtain these results, Lehman assumed for his cavity that at any frequency the number of electromagnetic modes, M, contained within the 3-dB bandwidth, was infinite.

In order to obtain PDFs for comparison with Lehman's $f(P_{idB})$, we have measured the magnitude of S_{21}, in dB, for our chamber, using a receiving antenna and then again using a D-dot sensor. The antenna is linearly polarized and thus responds to one component of **E**, E_i, away from the chamber walls; and the D-dot sensor is mounted directly on a wall and so also responds to only one component of **E**. Our results for antenna and sensor are very similar, and we have included here only those for the sensor. Fig. 3 shows the PDF for our highest frequency, 10.0 GHz, and Fig. 4 the PDF for the lowest, 1.0 GHz. We used 153 observations (paddle wheel positions) and a 1/4-dB interval size to construct the histograms. Both figures also show, as the smooth curve, Lehman's $f(P_{idB})$ from Eq. 7. Notice that the general histogram shape for 10.0 GHz displays much better agreement than the one for 1 GHz with Lehman's curve. The same is true of the standard deviation values, the 10-GHz σ being closer to 5.57 dB. This effect is perhaps not surprising, since Lehman took $M \rightarrow \infty$; and we have a much larger M value at 10 GHz, where M = 32, than at 1 GHz, where M = 0.3. To obtain these values we used the equation [7]

$$M = 8\pi V/(\lambda^3 Q) \quad (8)$$

where λ is the wavelength of the microwaves and the values of Q were taken from Fig. 2 (1.67×10^3 at 1 GHz and 1.42×10^4 at 10 GHz).

Although we have not yet performed goodness-of-fit tests on our PDFs, it appears, on the basis of the results in Fig. 3, that at the higher frequencies our chamber fits Lehman's theoretical model. Indeed, Gustav Freyer [8] has found that many other chambers do also; and, in view of this, the chambers provide a universal environment in which to carry out EMC tests. For the lower frequencies, however, Fig. 4 shows us that our PDF clearly deviates from Lehman's. It would be useful in the future to characterize this region more fully and determine the implications, for EMC testing, of the change in PDF. But we can already answer this question: As the operating frequency of a chamber is lowered so that the number of modes, M, is no longer large, does this cause the distribution of EM power density values to become narrower? The answer is, for our chamber at least: no; the distribution actually *widens* as the number of modes decreases, as shown by the increase in standard deviation from 5.4 to 8.6 dB.

One additional point is significant. The use of our wall-mounted sensors marks the first time, to our knowledge, that Lehman's model for the EM power density has been experimentally verified on the wall of a reverberation chamber rather than far away from it. This means that, in setting up an EMC immunity test in a reverberation chamber, for example, one can expect to expose the device under test to the *same* distribution of power density values at the wall as away from it.

V. CHAMBER SPATIAL CORRELATION FUNCTION

A. Theory In order to provide a complete statistical description of the fields in his complex cavity, Lehman [7] computed, in addition to the PDF, the spatial correlation function, κ. This function gives the cross correlation between P_i values at any two spatial points; it is defined in the standard way as

$$\kappa[P_i(\mathbf{r}_1)P_i(\mathbf{r}_2)] = \frac{e\{[P_i(\mathbf{r}_1) - \overline{P}_i(\mathbf{r}_1)][P_i(\mathbf{r}_2) - \overline{P}_i(\mathbf{r}_2)]\}}{\sqrt{e\{[P_i(\mathbf{r}_1) - \overline{P}_i(\mathbf{r}_1)]^2\}e\{[P_i(\mathbf{r}_2) - \overline{P}_i(\mathbf{r}_2)]^2\}}}$$

where $\mathbf{r}_1$ and $\mathbf{r}_2$ are two position vectors, $e\{X\}$ is the expected value of X, and $\overline{P}_i$ is the mean of P_i. Expressed in a sentence, κ is a measure of the degree to which the deviation from the average of the power density at one point in space is correlated with the deviation at another point.

Lehman found that κ is given by the rather simple expression

$$\kappa[P_i(\mathbf{r}_1)P_i(\mathbf{r}_2)] = [\sin(kR)/(kR)]^2 \quad (9)$$

where $R = |\mathbf{r}_1 - \mathbf{r}_2|$ = spacing between points and $k = 2\pi/\lambda$. The behavior of κ as a function of R is as follows: $\kappa = 1.0$ for $R = 0$, then falls to zero when $kR = \pi$, and thereafter remains very small. Thus the concept of "correlation length" applies; and the value of R for which $kR = \pi$ may be taken as the correlation length, R_{corr}, or the approximate length over which the power density is correlated. This value is $R = R_{corr} = \lambda/2$.

B. Measurement The spatial correlation function has not previously been measured inside a reverberation chamber. We chose to carry out the measurement on a wall of our chamber by utilizing two identical D-dot sensors and varying the spacing between them. This arrangement, which we refer to as chamber configuration 3, is illustrated in Fig. 5. The

following nine spacing values were used: 0.5, 1.0, 1.5, 2.5, 5.5, 8.0, 11.5, 13.5, and 17.5 cm. Our measured values of P_i were substituted into the following standard formula for the estimate of κ:

$$\kappa[P_i(\mathbf{r}_1)P_i(\mathbf{r}_2)] = \frac{\sum_{n=1}^{N}[P_{in}(\mathbf{r}_1) - \overline{P}_i(\mathbf{r}_1)][P_{in}(\mathbf{r}_2) - \overline{P}_i(\mathbf{r}_2)]}{\sqrt{\sum_{n=1}^{N}[P_{in}(\mathbf{r}_1) - \overline{P}_i(\mathbf{r}_1)]^2 \sum_{n=1}^{N}[P_{in}(\mathbf{r}_2) - \overline{P}_i(\mathbf{r}_2)]^2}} \tag{10}$$

where $\overline{P}_i(\mathbf{r}_1) = \frac{1}{N}\sum_{n=1}^{N} P_{in}(\mathbf{r}_1)$, $\overline{P}_i(\mathbf{r}_2) = \frac{1}{N}\sum_{n=1}^{N} P_{in}(\mathbf{r}_2)$, and N = number of observations = 200.

The requirement for taking data from two sensors in the SCF measurement created a new instrumentation problem for us because the network analyzer has only one input port. We solved this problem by purchasing a coaxial switch, which is shown in Fig. 5, to connect the sensors alternately to the network analyzer. To run the switch, we added a separate DC power supply and another interface board in the computer. Our data-taking program was modified to provide computer control of the switch as well as the analyzer and paddle wheel.

C. Numerical Simulation A computer simulation of an SCF measurement inside a microwave reverberation chamber has been obtained by modeling the chamber as a rectangular cavity with one movable wall and no paddle wheel. This geometry, which greatly simplifies the electromagnetic boundary conditions by eliminating the paddle wheel, was suggested by Huang and Edwards [9]. As can be seen in Fig. 5, in our chamber the paddle wheel is located just below the top; so for the "moving wall" approach, SCF measurements are simulated using a set of rectangular cavities with tops that vary in equally spaced increments from the lower edge of our paddle wheel to the top of our chamber.

The moving wall algorithm is implemented with certain pre-processing steps in order to shorten overall execution times. These steps involve the calculation, sorting, and archival of a large number of resonant frequencies for all of the rectangular cavities that are to be considered in the calculations. In the present case, a simulation of a chamber experiment with 200 distinct paddle wheel positions is desired, and resonant frequency arrays are calculated using the following equation [10] for 200 rectangular cavities:

$$f_{mnp} = (c/2)[(m/a)^2 + (n/b)^2 + (p/d)^2]^{1/2}$$

where m, n, and p are integers and a, b, and d are cavity dimensions in the x, y, and z directions, z being vertical. The lengths and widths, a and b, of the cavities are all the same as those of the chamber. The heights, d, of the cavities vary in increments of $(d_{max} - d_{min})/200$, from a minimum value, d_{min} (paddle wheel lower edge height), to a maximum, d_{max} (chamber height). For each height, a resonant frequency array is determined by varying (m,n,p) from (1,1,0) to some suitably large final values, such that all of the resonances in a particular frequency interval are included. The initial values of n and m are unity instead of zero since in this particular study the D-dot sensors are mounted on the bottom of the chamber (as indicated in Fig. 5) and thus detect only the z-component of the electric field, which from Eq. 13 below can be seen to be identically zero when n or m is zero.

The simulation program processes the sorted resonant frequency data generated by the pre-processing program. It first determines a set of significant resonances, or modes, at a particular simulation frequency, f, for a specific cavity height. These modes are selected by

modeling the frequency response of each cavity resonance as a second-order-circuit response given by $F(j\omega)$ in Eq. 11.

$$F(j\omega) = \omega_{mnp}^2/[(j\omega)^2 + (\omega_{mnp}/Q_{net})j\omega + \omega_{mnp}^2)] \tag{11}$$

where $\omega = 2\pi f$, $\omega_{mnp} = 2\pi f_{mnp}$, and $Q_{net} = Q$ of the chamber. The program scans the appropriate resonant frequency array for the resonance that is closest to the simulation frequency,evaluates its magnitude at this frequency using Eq. 11, and stores the magnitude as a variable called mag1. The magnitudes associated with other neighboring resonances are evaluated successively, at the simulation frequency, in ascending and descending frequency order until resonances are encountered that generate a magnitude that is less than 0.1*mag1, at which point the mode selection process is terminated. The results of this process are sets of mnp indices, together with amplitudes, that correspond to modes that significantly contribute to the simulated chamber response at the chosen simulation frequency.

If more than one receiving D-dot sensor is used, as in the present case where there are two, then Q_{net} , the overall theoretical Q of the chamber, is calculated from Eq. 6 modified to account for the number of sensors, η:

$$Q_{net} = \left(\eta/Q_{\dot{D}} + 1/Q_{eqv}\right)^{-1}. \tag{12}$$

The $1/Q_{eqv}$ term in this equation expresses the loading due to the chamber walls, while the $\eta/Q_{\dot{D}}$ term gives the loading due to the sensors.

The z-component of the electric field for each mnp mode is given by the solution [3] of the boundary-value problem for the rectangular cavity as follows:

$$\begin{aligned} E_z &= A_{TE}\sin(k_x x)\sin(k_y y)\cos(k_z z) \\ &\quad + A_{TM}\exp(j\theta)\sin(k_x x)\sin(k_y y)\cos(k_z z) \end{aligned} \tag{13}$$

where $k_x = \frac{m\pi}{a}$, $k_y = \frac{n\pi}{b}$, $k_z = \frac{p\pi}{d}$, and θ is a random angle between 0 and 360 degrees. Here, the first term represents the TE solution whereas the second term represents the TM. The amplitudes A_{TE} and A_{TM} are determined by the manner in which the modes are excited by the transmitting antenna, which is not known; thus we have just taken $A_{TE} = A_{TM} = 1$. Likewise the phase difference between the terms, θ, depends on the excitation and is not known; so we have made θ random, with uniform distribution between zero and 360 degrees. Eq. 13 is evaluated for all of the selected mnp sets and is multiplied by the corresponding magnitude factor from the selection step. The results are summed to yield the total electric field (z-component), and a power density sample is obtained by taking the magnitude-squared of the total field.

In the simulation program, the process of calculating power density samples is embedded inside two nested loops. The outer loop is the "height-perturbation loop" where a resonance frequency array corresponding to a particular cavity height is loaded into memory from disk storage. The inner loop is the "frequency loop" where a pre-determined initial simulation frequency is incremented by a specified amount. Two power density calculations are performed within the inner loop, one for the location of each of the two sensors on the bottom of the chamber. This procedure generates two power density samples for each simulation frequency and each rectangular cavity height. The power density data is stored in two large memory segments, one segment for each spatial location. A computer-generated

spatial correlation function output is obtained by correlating the data in the two memory segments using Eq. 10.

The implementation of the moving wall algorithm is a set of MATLAB M-files that execute on a SUN10 SPARC workstation. Two main M-file programs perform the actual calculations while a set of small M-files, that are called by the main programs, perform auxiliary calculations such as evaluation of the Q_{net} formulas (Eq. 12), evaluation of (second-order response) magnitudes (Eq. 11), and generation of mnp integers. The first main program calculates, processes, and stores, on disk, approximately 150 megabytes of resonant frequency data. The second main program processes this data in segments and generates a simulated SCF output. The most significant array sizes in this program, at any given time during the execution process, are three approximately 1,000,000-element mnp integer arrays, one 50,000 to 75,000-element integer array segment of resonant frequency data, one 50,000 to 75,000-element double-precision array segment of resonant frequency data, and two 51 x 200-element double-precision arrays with calculated power density samples.

D. Results In Fig. 6 we present the results of our study of the spatial correlation function. Graphs of SCF versus spacing are shown for 51 different microwave frequencies, covering the range from 1.0 GHz to 13.5 GHz in 0.25 GHz steps. Each graph contains three curves: the theoretical SCF from Lehman's complex cavity, the measured SCF from the bottom wall of our reverberation chamber, and the simulated SCF from the bottom wall of our moving-wall computer model. Thus a three-way comparison is provided, encompassing theory, experiment, and simulation.

It can been seen from Fig. 6 that the general behavior of the SCFs is to fall from an initial value of unity at zero spacing to a small value as the spacing is increased, the fall-off proceeding more rapidly at the higher frequencies. Note that the measured and simulated SCFs in Fig. 6 are plotted for only ten spacings: 0, 0.5, 1.0, 1.5, 2.5, 5.5, 8.0, 11.5, 13.5, and 17.5 cm.

Further inspection of the curves in Fig. 6 reveals the following facts:

(1) In general, there is enough agreement among all three types of SCF (theory, experiment, and simulation) to suggest that no egregious errors have been committed.

(2) For the middle and higher frequencies, there is good agreement among the SCFs, which means that the correlation length, $R_{corr} = \lambda/2$, discussed theoretically in part A above is applicable in practice.

(3) For the middle and higher frequencies and larger spacings, the measured and simulated SCFs do not lie as close to zero as the theoretical SCF does; but they are nonetheless quite small and, with statistical fluctuations, lie in the range $\pm$ 0.2.

(4) For the lower frequencies and larger spacings, the measured and simulated SCFs tend to be significantly higher than the theoretical SCF. This lack of agreement with Lehman's theory is not surprising because the chamber mode density is so low at these frequencies, and, furthermore, we have already seen in section IV a lack of agreement with Lehman's PDF in this situation. As mentioned in section IV, our chamber has $M = 0.3$ at 1.0 GHz, while Lehman assumed $M \rightarrow \infty$. In addition, we know that our SCF ought to be quite high because, with only a small number of modes, there is little chance for the occurrence of the cancellation that is required to produce a low SCF.

At these lower frequencies the correlation length is excessively large, $R_{corr} > \lambda/2$, or perhaps even nonexistent in some cases (e.g. 2.00 GHz) where there is a periodic oscillation rather than a steady decline in the correlation function.

E. Comments and Conclusions An important parameter embedded in the simulation of the SCF is the theoretical Q of the chamber, Q_{net}, given in Eq. 12. This parameter can easily be altered if desired-- lowered by varying degrees for example, to test the effect on the SCF of various amounts of chamber loading. For the results in Fig. 6 we have in fact altered Q_{net} by dividing it by 10, thus giving a Q more in line with what we measured earlier ($\sim Q_{net}/7$), as discussed in section III and shown in Figs. 1 and 2.

For the middle and higher frequencies, the good agreement we see among all three types of SCF (fact (2) above) indicates that our laboratory chamber and our simulated chamber are behaving much like Lehman's complex cavity. In the case of the laboratory chamber the complexity is probably introduced by the paddle wheel. In the simulated chamber the complexity may be due to our assumption of random phase for the TM modes relative to the TE (Eq. 13), but this point needs further investigation. In fact, additional insight into chamber behavior can probably be obtained by further development of our simulation technique. It seems remarkable that a technique which does not directly model the paddle wheel is capable of such an accurate simulation of the measured SCF.

The mutual agreement of the SCFs (fact (2) above), along with the agreement observed for the PDFs in section IV, completes the validation of Lehman's statistical theory in so far as it applies to reverberation chambers.

Our confirmation of the existence of a correlation length, R_{corr}, should be good news for those who wish to employ a reverberation chamber to simulate the fields impinging on a device located inside a metal compartment of some sort. The geometry of the compartment will not need to be reproduced completely in the chamber but only over the distance R_{corr} around the device.

Using the SCF plots at discrete frequencies given in Fig. 6, we have tried to pinpoint the minimum frequency at which the measurements agree with the theory (fact (2) above). Although our evaluation is somewhat subjective, we feel safe in stating that the low-frequency limit of the chamber, from the standpoint of attaining a good approximation of the ideal SCF, lies at 3.0 GHz. This conclusion may actually have rather wide-reaching consequences because 3.0 GHz is considerably higher than the values obtained from current guidelines for the operation of reverberation chambers for EMC testing. These guidelines suggest a low-frequency limit of either the 60-mode frequency [2], which is only 844 MHz in our chamber, or of 6 times the lowest resonance frequency [17], which is only 1.41 GHz in our chamber. Thus it may be that the current guidelines are not stringent enough (or perhaps too simplistic).

VI. SUGGESTIONS FOR FUTURE RESEARCH

A. Relatability Traditional EMC testing has involved the use of anechoic chambers, open area test sites, and TEM cells [12]. For checking immunity, the device under test (DUT) is illuminated with a single EM wave from a powerful, wide-band source, and the response of the DUT is noted as it is re-positioned many times to receive the incident radiation from different angles and with different polarizations. This is a time-consuming

and costly process. In addition, capital-equipment costs are extreme, especially for anechoic chambers and high-power microwave sources. But these systems have the important attribute of simulating the common real-world situation of an interfering signal, often a single plane wave, impinging on the device.

An alternative to these systems is the reverberation chamber-- a metal enclosure forming a high-Q cavity supporting many simultaneous electromagnetic modes. It can serve for both immunity and emissions testing [13]. Data acquisition with a reverberation chamber is much faster than with the other systems because, with so many modes, the chamber exposes the DUT to a great variety of incident fields and polarizations without the need for re-positioning. Also, much less source power is required than in the other systems because of the energy intensification resulting from the high Q. A further advantage, compared to an anechoic chamber, is the absence of expensive absorbing material.

Although there is a tremendous potential cost benefit associated with reverberation chambers, there are currently only about twenty chambers worldwide [14] employed for EMC testing. The main problem with them is how to relate test results obtained with multiple simultaneous waves to the actual single-plane-wave threat situation. What is needed to solve this "relatability" problem is a coordinated program featuring experiments and rigorous numerical modeling. Frederick Tesche has suggested [15] that a good way to begin would be to consider fairly simple DUTs such as transmission-line structures and compare the probability distribution of the responses in a chamber to the probability distribution of the responses to single plane waves.

B. Important Parameters In order to have sufficient field complexity for use as an EMC test chamber, a reverberation chamber must exhibit a large enough number of simultaneous modes at the test frequency and it must have a paddle wheel which is big enough [16] to significantly alter the modes as it rotates. The effective number of simultaneous modes, M, is given by Eq. 8 and can be written as

$$M = 8\pi V/(\lambda^3 Q) \sim 8\pi(L_{Ch}/\lambda)^3/Q,$$

where V is the volume of the chamber, λ is the wavelength of the microwaves, Q is the Q of the chamber, and L_{Ch} is a typical dimension of the chamber. Thus for EMC testing we need M greater than some minimum value, M_{min}; or $L_{Ch}/\lambda > (L_{Ch}/\lambda)_{min}$ and $Q < Q_{max}$. But another constraint on Q is that it cannot be too small, or else there will not be adequate reverberation and the effectiveness of the paddle wheel will be reduced. Thus $Q > Q_{min}$. And as noted above, the paddle wheel size, L_{PW}/λ, must be larger than $(L_{PW}/\lambda)_{min}$. Thus the complete set of requirements for the chamber is as follows:

$$L_{Ch}/\lambda > (L_{Ch}/\lambda)_{min}$$
$$Q_{min} < Q < Q_{max}$$
$$L_{PW}/\lambda > (L_{PW}/\lambda)_{min}$$

There is one additional constraint which has to do with the data-taking procedure; the number of observations must be sufficient; $N > N_{min}$.

Note that the first requirement says that there is a minimum chamber size, measured in wavelengths. This can be used in two ways: either to decide on the size of the smallest usable chamber if the frequency is given, or to decide on the lowest usable frequency if the chamber is given. In any case one would want to determine $(L_{Ch}/\lambda)_{min}$ on the basis of some

specific criterion, such as having no more than a ±3 dB spatial variation in the average field in the chamber.

The important parameters $(L_{Ch}/\lambda)_{min}$, Q_{min}, Q_{max}, $(L_{PW}/\lambda)_{min}$, and N_{min} are somewhat interrelated and may even depend on the characteristics of theDUT and the type of test being done. Finding general expressions for them would constitute a worthwhile project.

VII. PERSONNEL

A number of Texas Tech electrical engineering students have worked with Prof. Trost and PhD student Mitra to make significant contributions to this project. The graduate students were B. Esen and M. Ramesh. The undergraduates were A. Alvarado, S. Ayloo, K. Kelley, J. Ledbetter, S. Mikus, and P. Terry.

VIII. PUBLICATIONS RESULTING FROM THIS RESEARCH

1. T.F. Trost, et al., "Characterization of a Small Microwave Reverberation Chamber," presented by Prof. Trost at the 11th International Zurich Symposium on EMC in March, 1995, and appearing in the symposium proceedings, pp. 583-586.
2. A.K. Mitra and T.F. Trost, "Power Transfer Characteristics of a Microwave Reverberation Chamber," to appear in May, 1996, issue of *IEEE Transactions on Electromagnetic Compatibility.*
3. Mitra and Trost expect to submit for publication in the near future the results from this report and from Mitra's PhD thesis dealing with spatial correlation in reverberation chambers.

REFERENCES

1. P. Corona, *et al.*, "Performance and Analysis of a Reverberating Enclosure with Variable Geometry," *IEEE Trans. Electromagn. Compat.*, vol. EMC-22, pp. 2-5, Feb. 1980.
2. M.L. Crawford and G.H. Koepke, "Design, Evaluation, and Use of a Reverberation Chamber for Performing Electromagnetic Susceptibility/Vulnerability Measurements," NBS Tech. Note 1092, Apr. 1986.
3. T.A. Loughry, "Frequency Stirring: An Alternate Approach To Mechanical Mode-Stirring For The Conduct Of Electromagnetic Susceptibility Testing," Phillips Laboratory Tech. Report 91-1036, Nov. 1991.
4. J.M. Dunn, "Local , High-Frequency Analysis of the Fields in a Mode-Stirred Chamber," *IEEE Trans. Electromagn. Compat.*, vol. EMC-32, pp. 53-58, Feb. 1990.
5. C.E. Baum *et al.*, "Sensors for Electromagnetic Pulse Measurements Both Inside and Away from Nuclear Source Regions," *IEEE Trans. Electromagn. Compat.*, vol. EMC-20, pp. 22-35, Feb. 1978.
6. A.K. Mitra and T.F. Trost, "Power Transfer Characteristics of a Microwave Reverberation Chamber," to appear in May, 1996, issue of *IEEE Trans. Electromagn. Compat.*
7. T.H. Lehman, "A Statistical Theory of Electromagnetic Fields in Complex Cavities," Phillips Laboratory Interaction Note 494, May 1993.
8. G. Freyer, consultant, Monument CO, private communication, 1995.

9. Y. Huang and D.J. Edwards, "An investigation of the electromagnetic field inside a moving-wall mode-stirred chamber", The 8th IEE Int. Conf. on EMC, Edinburgh, UK, pp. 115-119, Sept. 1992.

10. R. Plonsey and R.E. Collin, *Principles and Applications of Electromagnetic Fields*, New York, McGraw-Hill, 1961.

11. B.H. Liu and D.C. Chang, "Eigenmodes and the Composite Quality Factor of a Reverberating Chamber," NBS Tech. Note 1066, Aug. 1983.

12. M.T. Ma, *et al.*, "A Review of Electromagnetic Compatibility/ Interference Measurement Methodologies," *Proc. IEEE*, vol. 73, pp. 388-411, March 1985.

13. J.P. Quine *et al.*, "Distortion of Radiation Patterns Transmitted Through Attenuating Cover Panels and Shielding Gaskets-- Need for Reverberation Chamber Measurements of Total Leakage," IEEE EMC Symposium, Aug. 1994, Proceedings, pp. 285-290.

14. M.O. Hatfield, NSWCDD, private communication, 1995.

15. F.M. Tesche, consultant, Dallas TX, private communication, 1995.

16. D.I. Wu and D.C. Chang, "The Effect of an Electrically Large Stirrer in a Mode-Stirred Chamber," *IEEE Trans. Electromagn. Compat.*, vol. 31, pp. 164-169, May 1989.

17. "Environmental Conditions and Test Procedures for Airborne Equipment," RTCA/DO-160D, RTCA, Inc., in process.

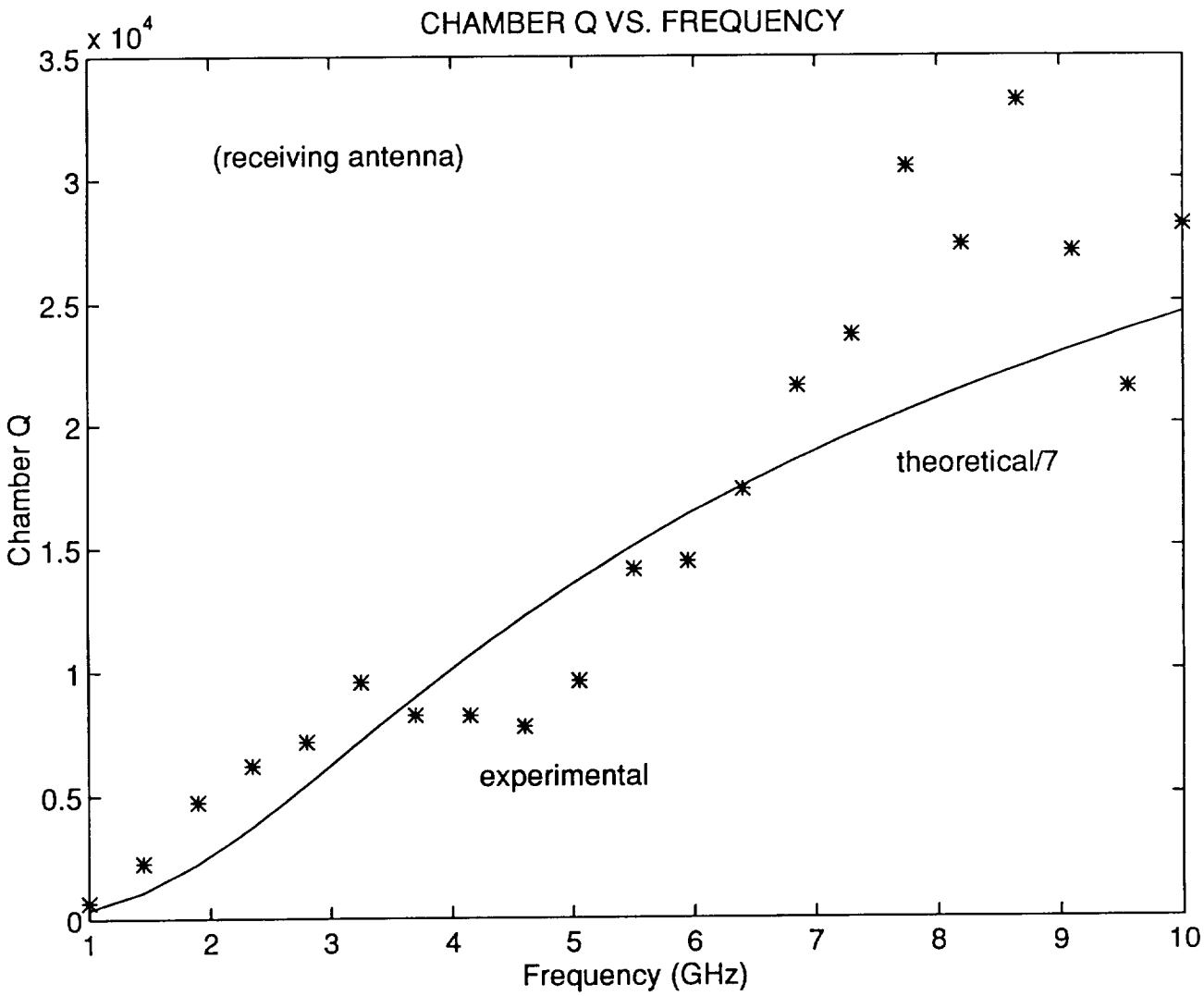

Fig. 1. Q of Texas Tech reverberation chamber in configuration 1 (receiving antenna).

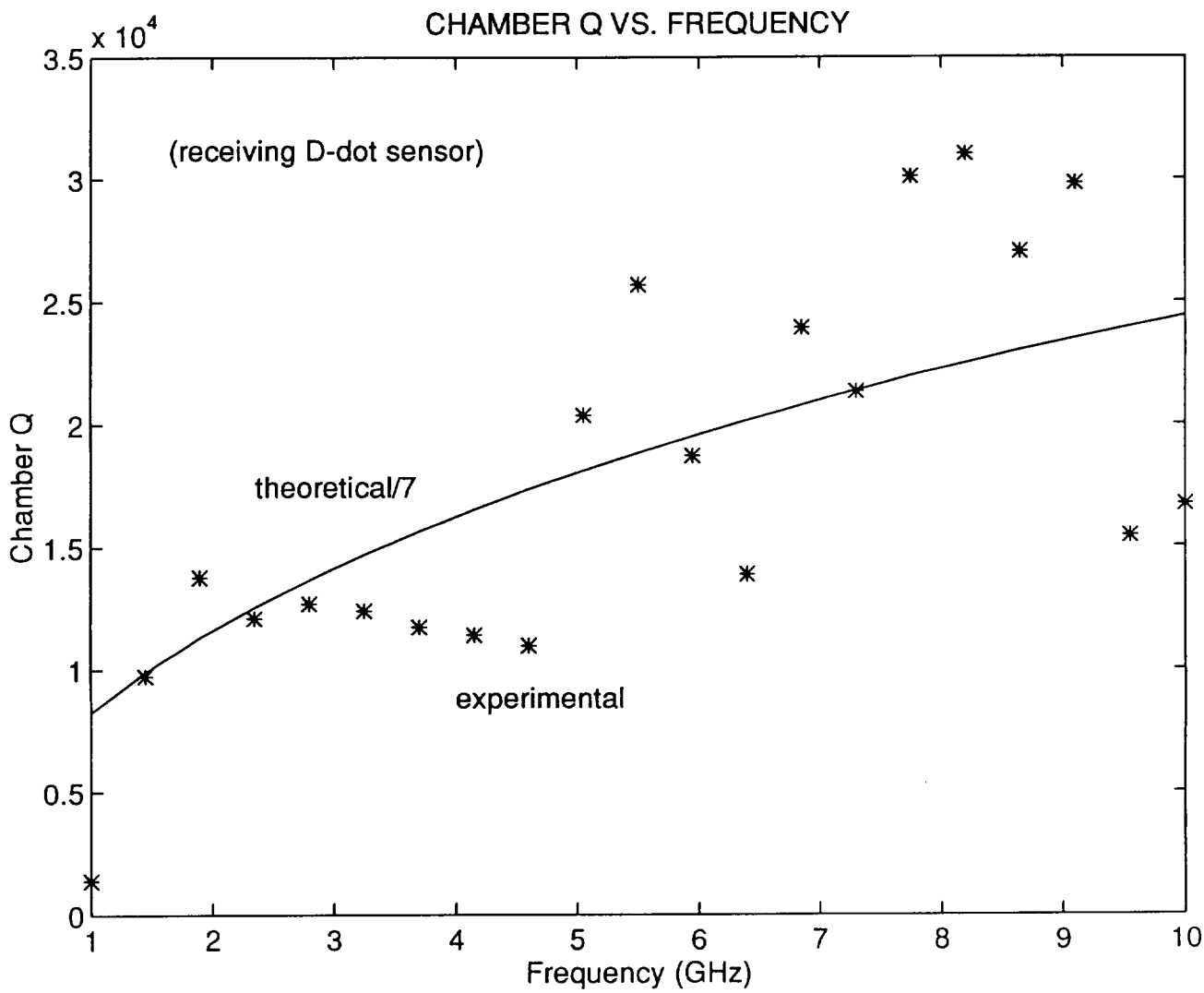

Fig. 2. Q of Texas Tech reverberation chamber in configuration 2 (receiving D-dot sensor).

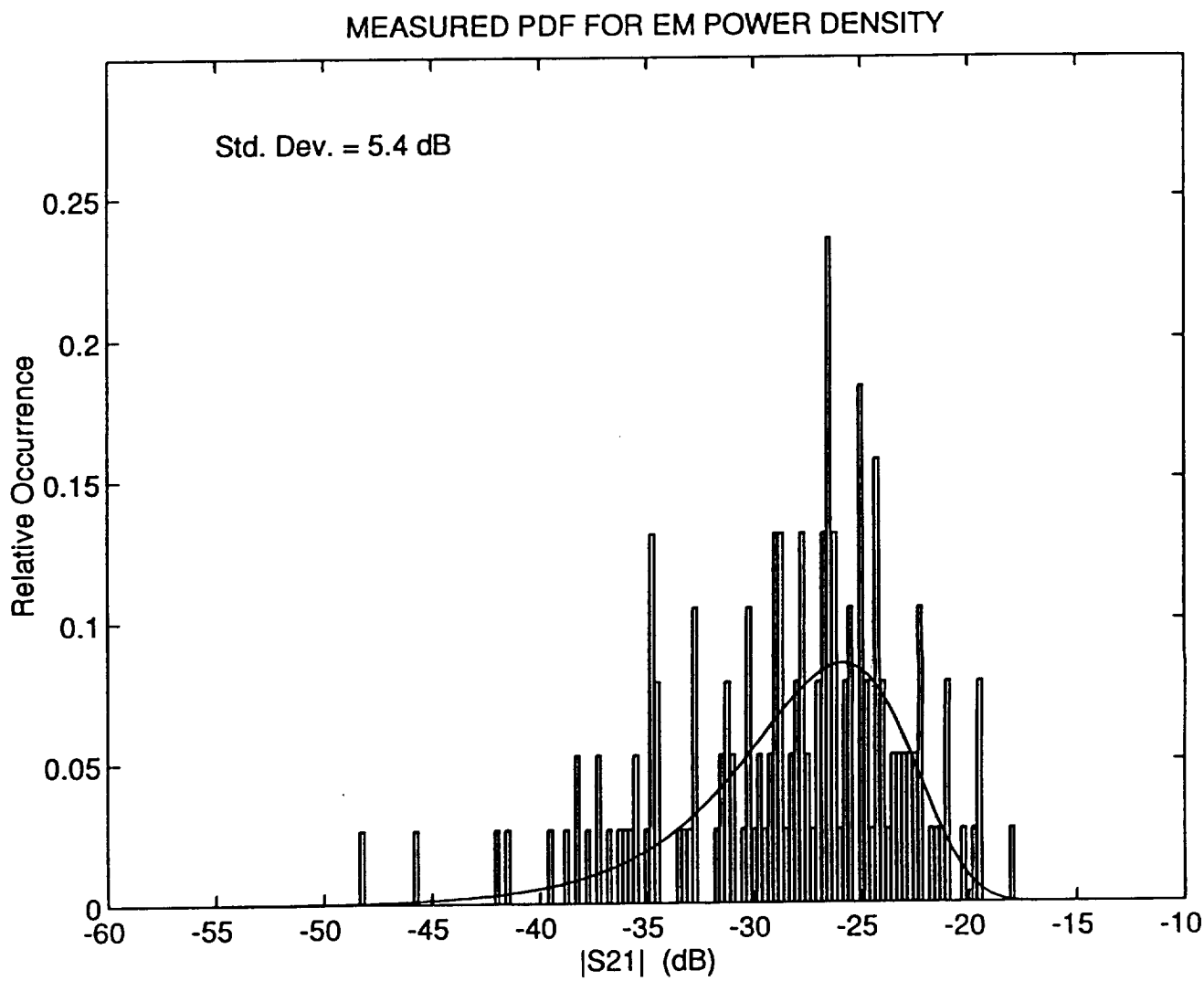

Fig. 3 Probability density function (PDF) at 10.0 GHz for configuration 2.

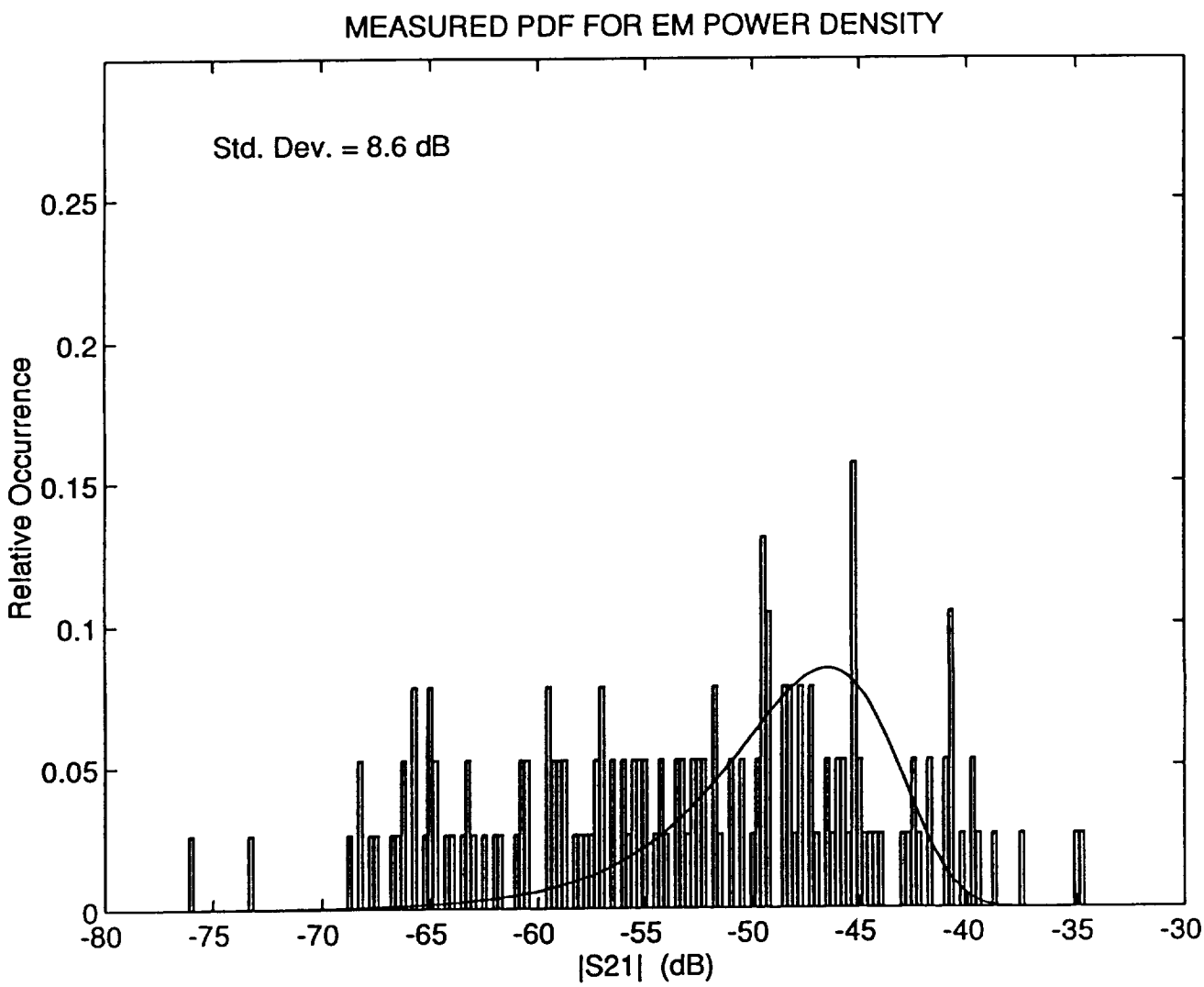

Fig. 4 Probability density function (PDF) at 1.0 GHz for configuration 2.

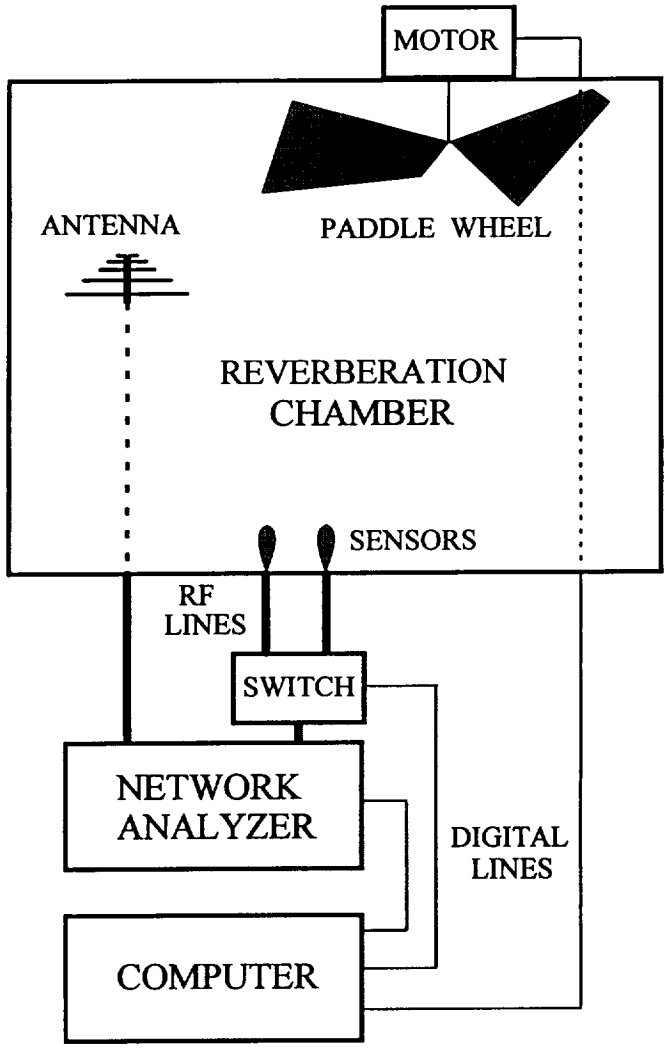

Fig. 5. Texas Tech reverberation chamber system in configuration 3 (two receiving D-dot sensors).

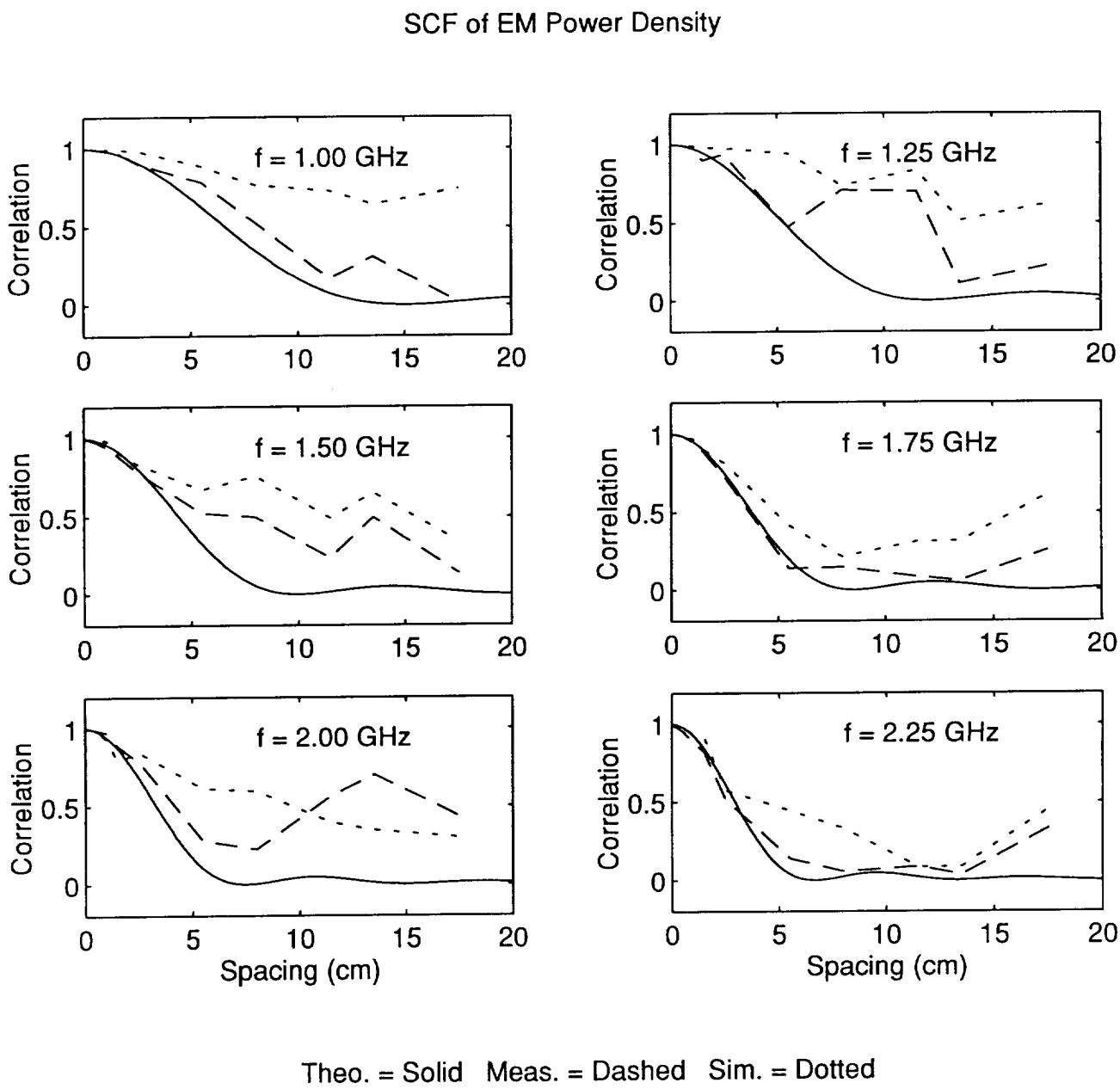

Fig. 6. Spatial correlation function (SCF) at various frequencies for configuration 3.

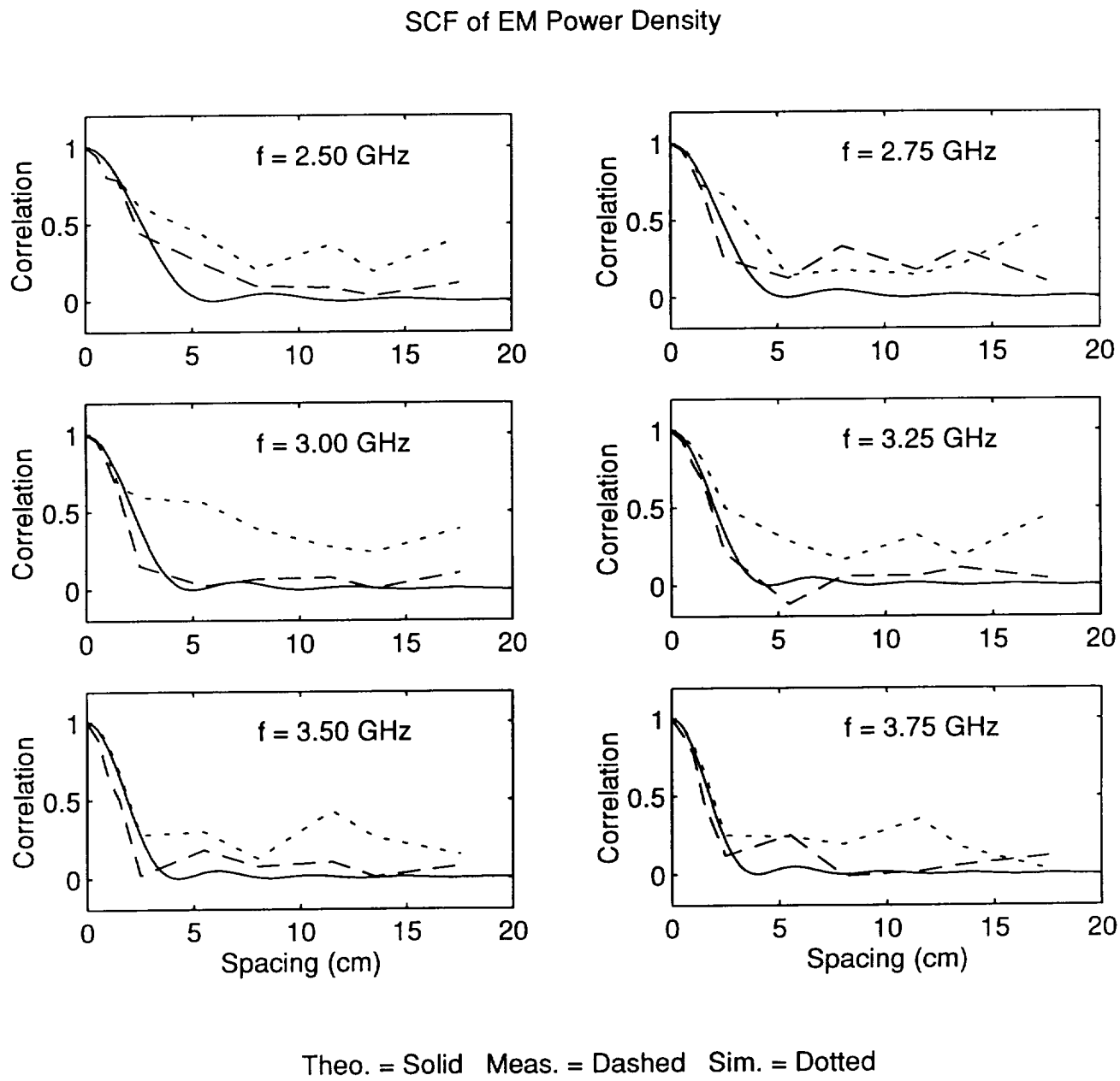

Fig. 6. Continued.

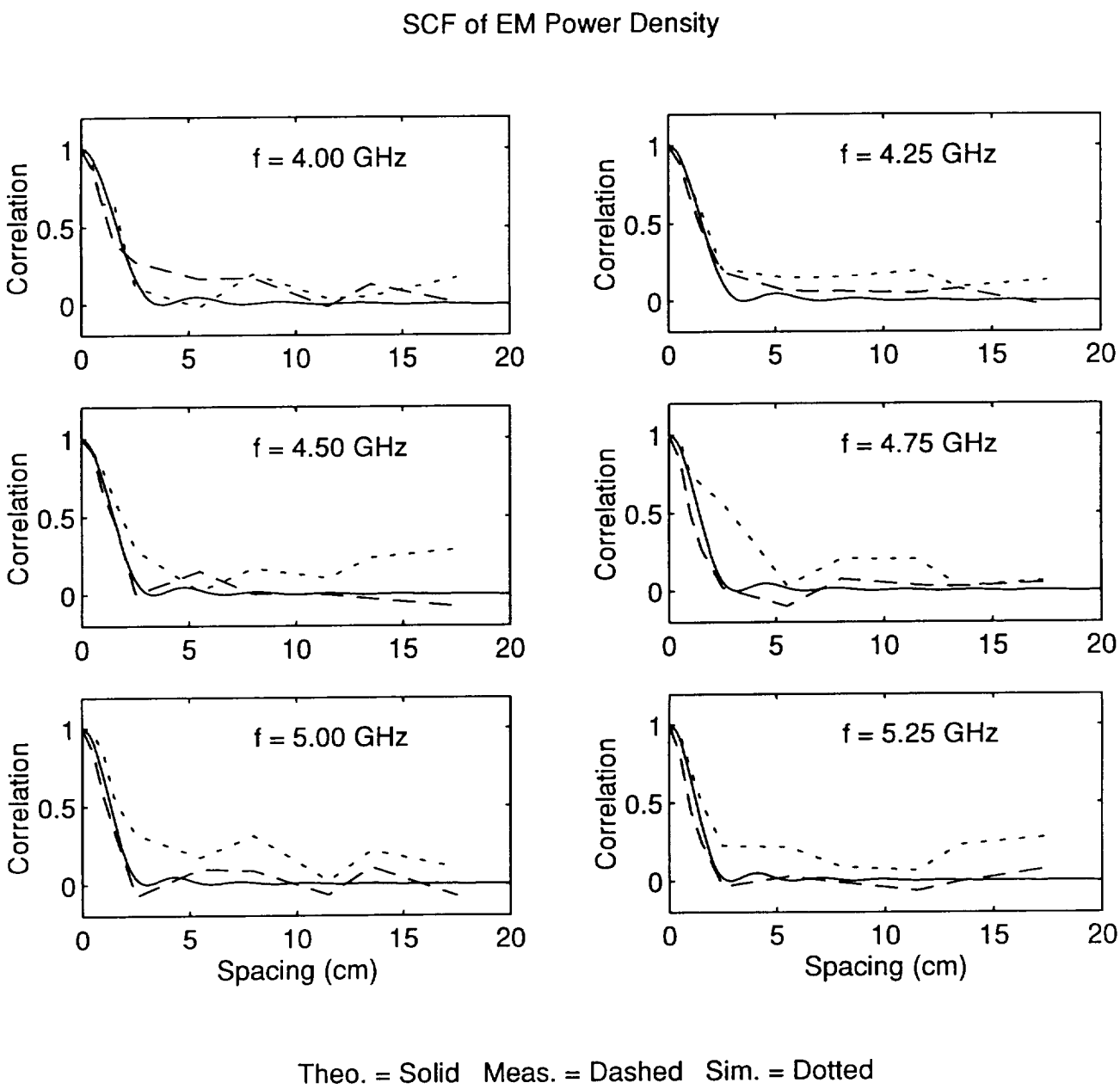

Fig. 6. Continued.

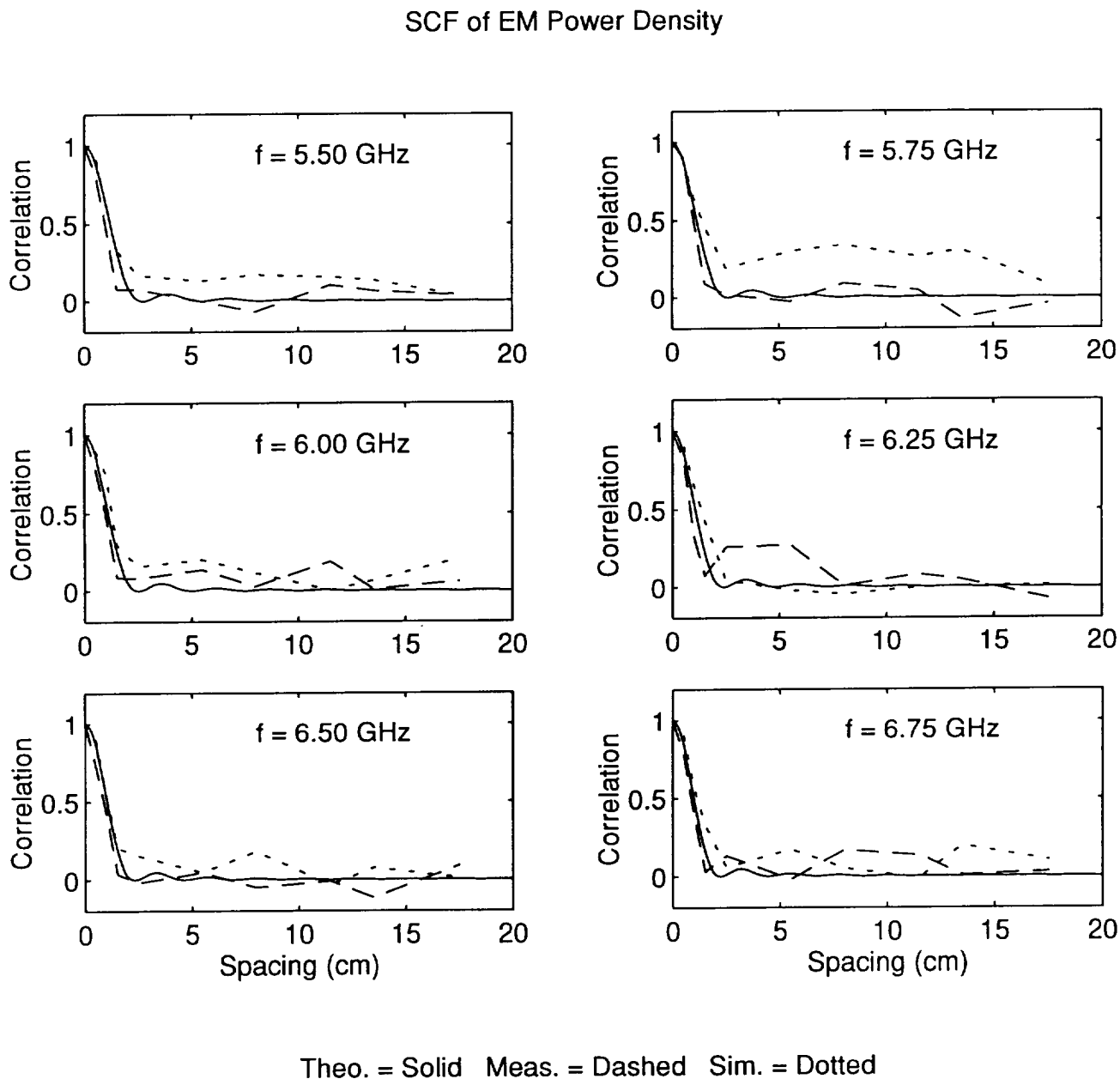

Fig. 6. Continued.

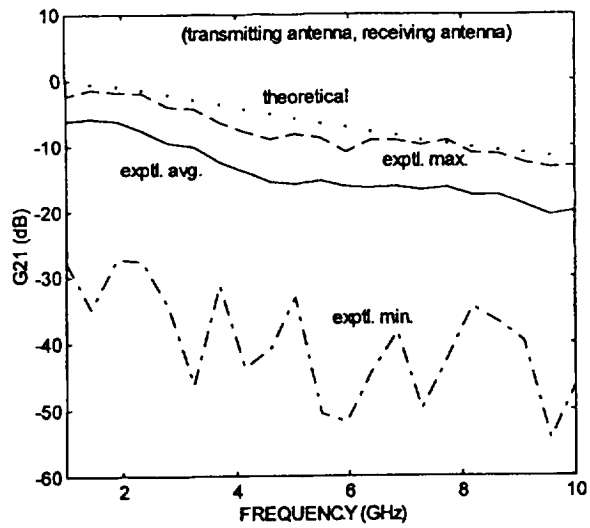

Fig. 2. Chamber gain versus frequency in configuration 1.

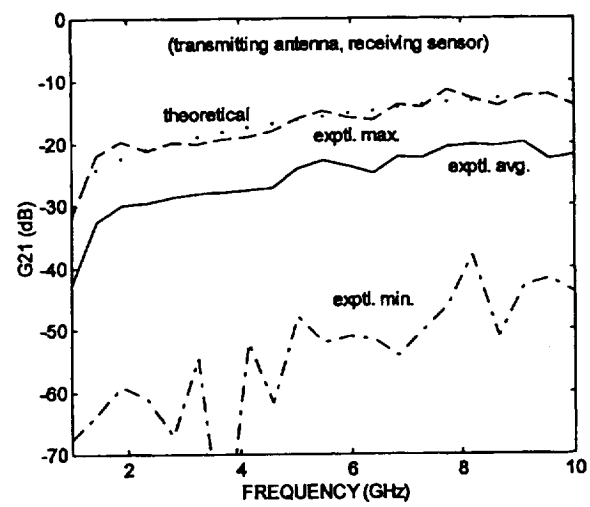

Fig. 3. Chamber gain versus frequency in configuration 2.

magnitude of the voltage transmission coefficient from port 1 to port 2, and $|S_{11}|$ is the magnitude of the voltage reflection coefficient at port 1. The $1 - |S_{11}|^2$ term is included to account for power returned to the source from the transmitting antenna. An important characteristic of the experimental curves in both Figs. 2 and 3 is the large, greater than 20 dB, difference between the maximum and minimum values of G_{21} over the entire frequency interval. This large difference is generally desirable with regard to proper reverberation chamber operation and is an indication of a properly functioning paddle wheel.

As might be expected, the theoretical curves in both Figs. 2 and 3 are only approximate representations of the actual response of the chamber. The slopes of the theoretical curves match the general trends of the slopes of the experimental maximum and average curves, but the theoretical values tend to be larger than the experimental. This discrepancy can perhaps be attributed to factors such as losses in the paddle wheel blades, antenna internal and mismatch losses, and losses through the access panel gasket, which were not modeled and included in the calculations. Regarding chamber wall losses, which were modeled, the value used for the wall conductivity, σ, was $2.32 \cdot 10^7$ S/m. Although this is the handbook value [11] for our particular aluminum alloy (6061T6), it may in fact be too high [8]; and this would add to the discrepancy.

Some insight into the physical phenomena that determine the shape of the chamber response can be obtained from an examination of equations used in the models. For example, for configuration 1 the $\omega^{2.5}$ dependence in the second term of the denominator of (9) can be attributed to the loading of the receiving antenna decreasing with ω^2 combined with the chamber wall loss increasing with $\omega^{1/2}$. Specifically, the ratio of Q's in (4) can be rewritten as a power ratio as follows:

$$\frac{Q_{\text{ant}}}{Q_{\text{eqv}}} = \frac{\omega W}{P_d} \Big/ \frac{\omega W}{P_{\text{eqv}}} = \frac{P_{\text{eqv}}}{P_d}. \tag{16}$$

Here, $P_d \propto \omega^{-2}$ from (7) and $P_{\text{eqv}} \propto \omega^{1/2}$ from (5) since $\delta \propto \omega^{-1/2}$.

At low frequencies, however, the first term in the denominator of (9) dominates. Thus, there are two distinct frequency regions. The transition point between these two regions can be calculated by setting the second term in the denominator equal to unity and solving for the corresponding value of ω. The result is a transition point for our chamber at 3.34 GHz. Below this transition point, $P_d > P_{\text{eqv}}$ in (16), so that power extraction from the chamber by the receiving antenna dominates over power loss to the chamber walls.

Similarly, for configuration 2 the $\omega^{-3/2}$ dependence in the second term of the denominator of (14) is due to the ω^2 variation in the $\dot{D}$-dot sensor loading combined with the $\omega^{1/2}$ variation in the chamber wall loss. (The frequency dependence of the sensor loading can be observed by solving for P_d in (13).)

The first term of the denominator of (14) becomes important only for high frequencies—well above 10 GHz for our particular chamber and sensor. This is the range where the power extracted by the sensor is dominant. Over the interval of our measurements, 1-10 GHz, the chamber wall loss dominates.

References

[1] D. A. Hill, "Electronic mode stirring for reverberation chambers," *IEEE Trans. Electromag. Compat.*, vol. 36, pp. 294-299, Nov. 1994.

[2] B. H. Liu and D. C. Chang, "Eigenmodes and the composite quality factor of a reverberating chamber," NBS Tech. Note 1066, Aug. 1983.

[3] M. L. Crawford and G. H. Koepke, "Design, evaluation, and use of a reverberation chamber for performing electromagnetic susceptibility/vulnerability measurements," NBS Tech. Note 1092, Apr. 1986.

[4] J. G. Kostas and B. Boverie, "Statistical model for a mode-stirred chamber," *IEEE Trans. Electromag. Compat.*, vol. 33, pp. 366-370, Nov. 1991.

[5] J. M. Dunn, "Local, high-frequency analysis of the fields in a mode-stirred chamber," *IEEE Trans. Electromag. Compat.*, vol. 32, pp. 53-58, Feb. 1990.

[6] T. F. Trost, A. K. Mitra, and A. M. Alvarado, "Characterization of a small microwave reverberation chamber," in *Proc. 11th Int. Zurich Symp. Tech. Exh. Electromag. Compat.*, 1995, pp. 583-586.

[7] T. A. Loughry, "Frequency stirring: An alternate approach to mechanical mode-stirring for the conduct of electromagnetic susceptibility testing," Phillips Laboratory Tech. Report 91-1036, Nov. 1991.

[8] D. A. Hill *et al.*, "Aperture excitation of electrically large, lossy cavities," *IEEE Trans. Electromag. Compat.*, vol. 36, pp. 169-178, Aug. 1994 .

[9] C. T. Tai, "On the definition of the effective aperture of antennas," *IEEE Trans. Antennas Propagat.*, vol. 9, pp. 224-225, Mar. 1961.

[10] C. E. Baum *et al.*, "Sensors for electromagnetic pulse measurements both inside and away from nuclear source regions," *IEEE Trans. Electromag. Compat.*, vol. 20, pp. 22-35, Feb. 1978.

[11] J. H. Potter, *Handbook of the Engineering Sciences*, vol. II. Princeton, NJ: Van Nostrand, 1967, p. 858.

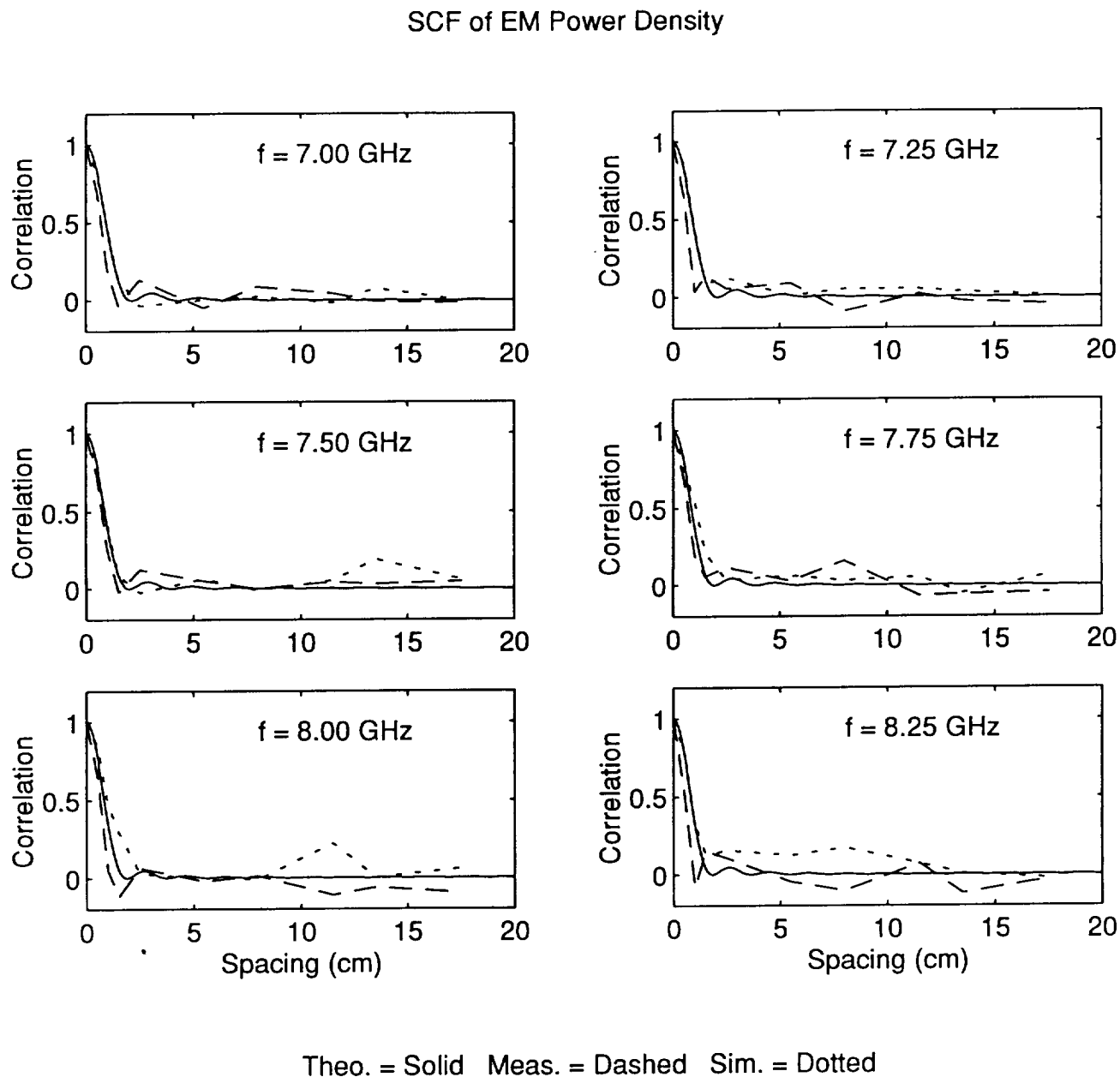

Fig. 6. Continued.

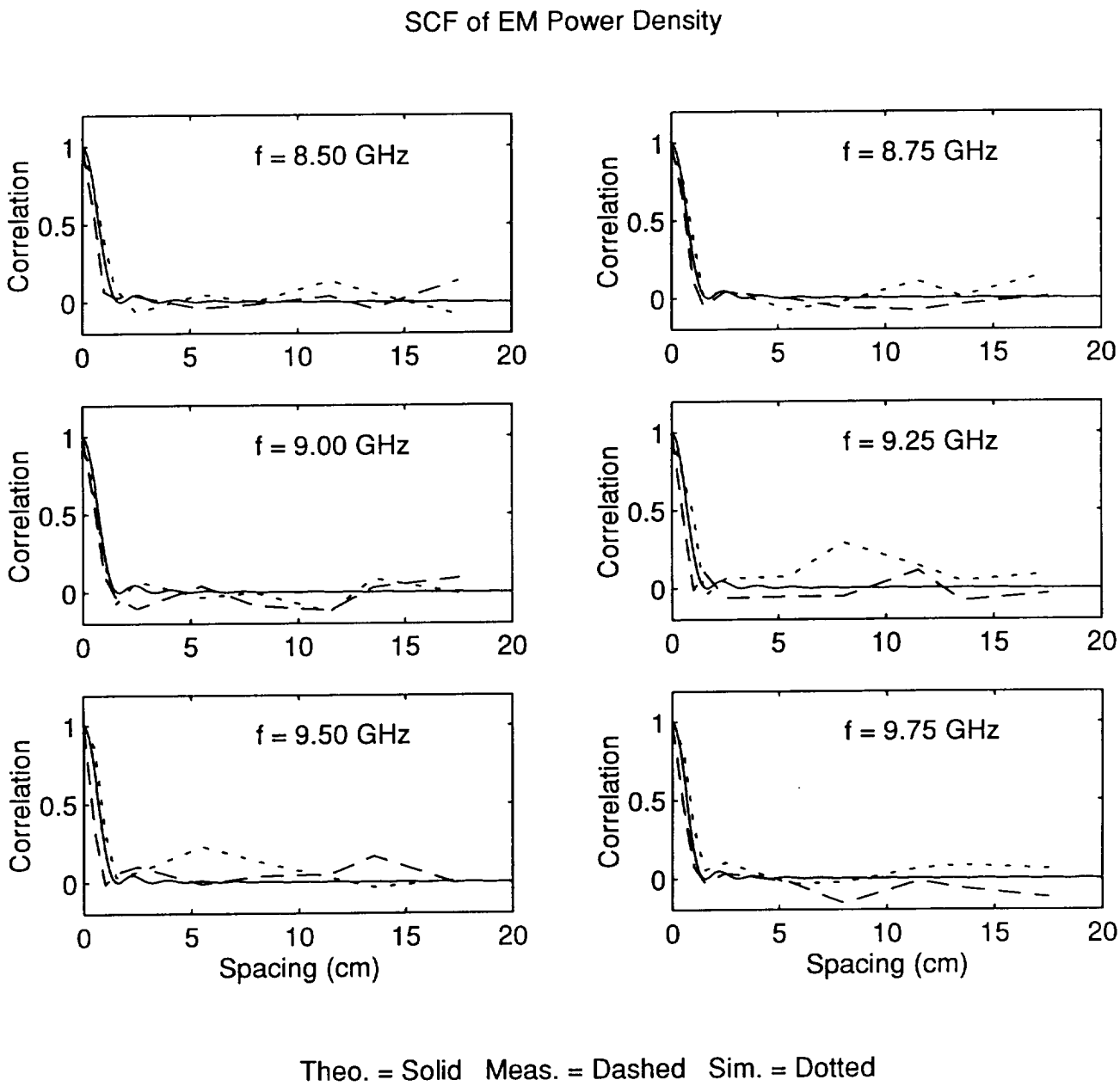

Fig. 6. Continued.

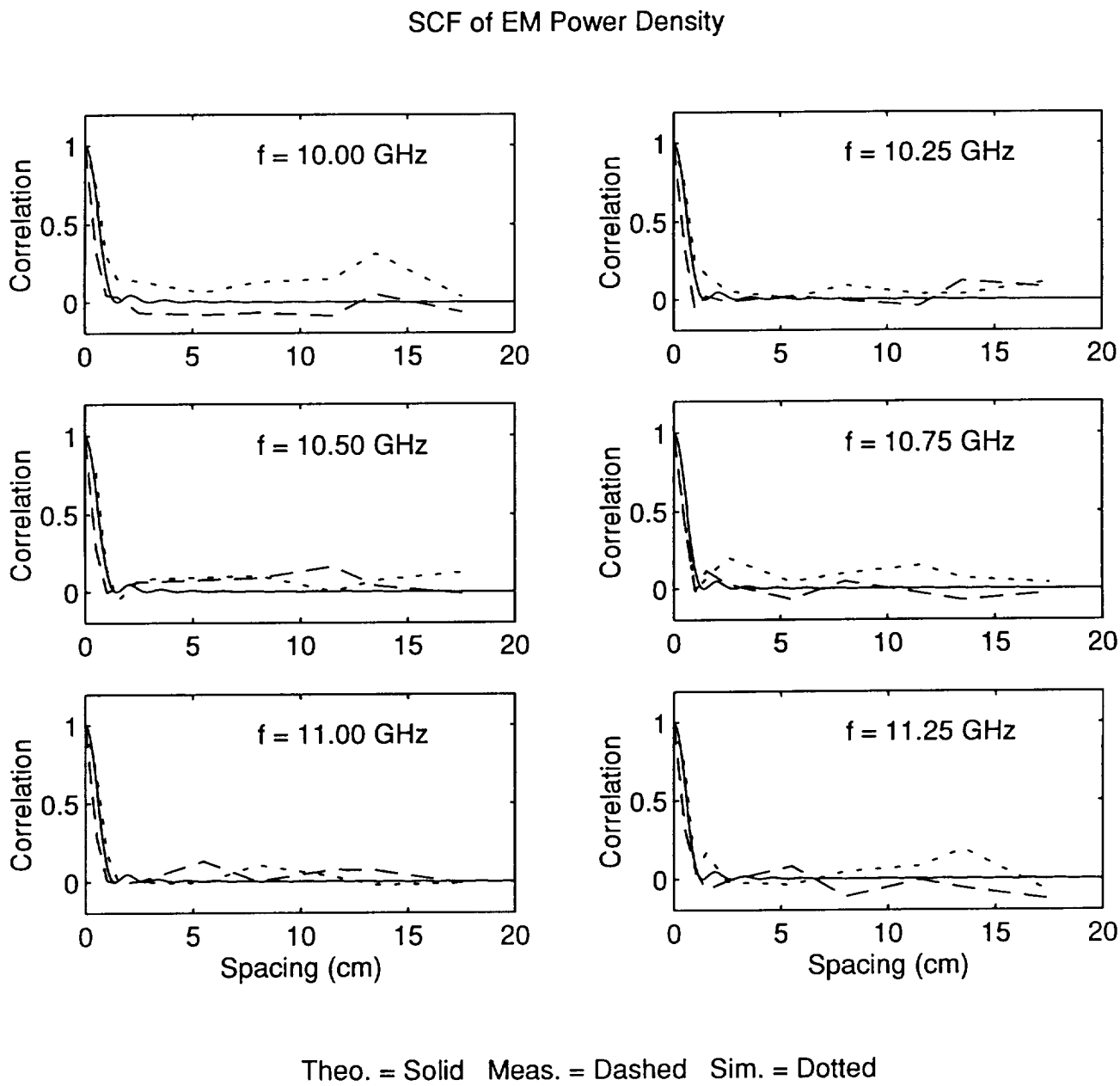

Fig. 6. Continued.

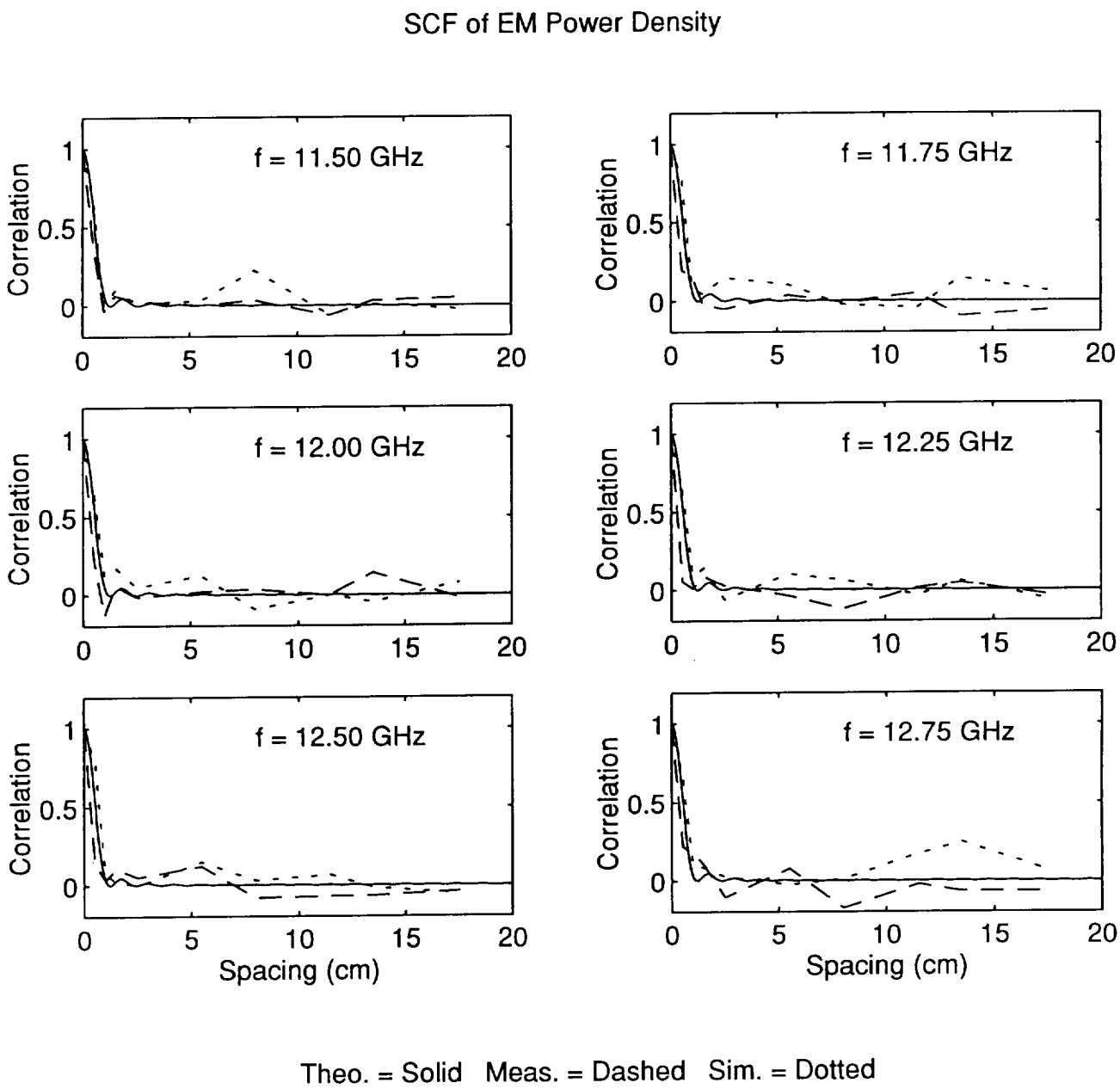

Fig. 6. Continued.

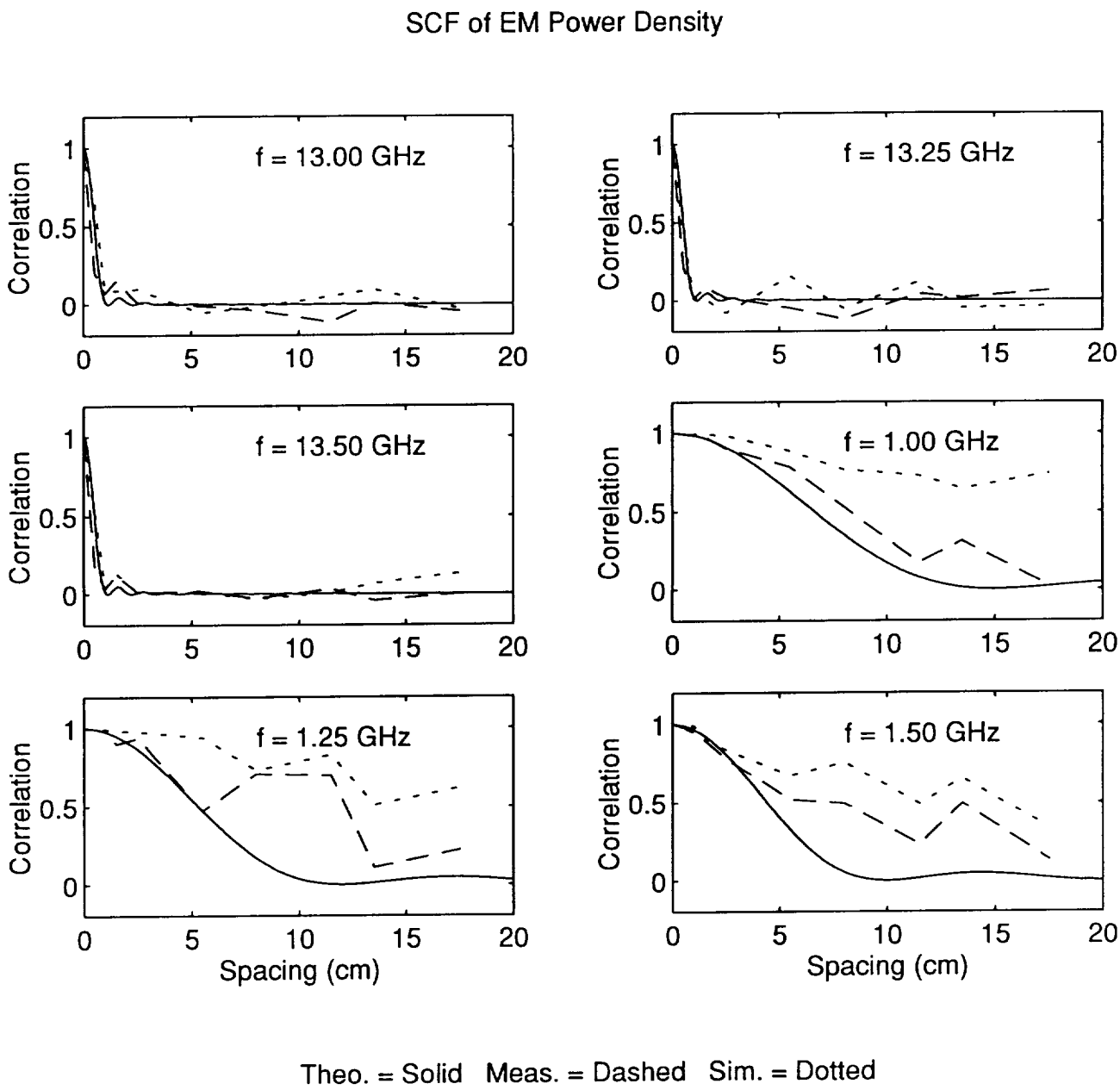

Fig. 6. Continued.

Short Papers

Power Transfer Characteristics of a Microwave Reverberation Chamber

Atindra K. Mitra and Thomas F. Trost

Abstract—**Power transfer through a microwave reverberation chamber is studied theoretically and experimentally. Two configurations are employed: In the first, the chamber contains a transmitting antenna and a receiving antenna; in the second, it contains a transmitting antenna and a receiving D-dot sensor. For each configuration a theoretical model is derived and laboratory measurements are carried out for the power gain of the chamber as a function of frequency. The models prove useful in predicting the observed variation of gain with frequency, and they provide insight into the importance of power flow to the chamber walls and to the receiving antenna/sensor.**

I. Introduction

The increasing popularity of microwave reverberation chambers for electromagnetic immunity testing applications has motivated a number of investigations [1]–[8] into the modeling of electromagnetic field-related quantities within the chamber. The chambers are generally associated with a number of desirable features, such as statistically uniform (or homogeneous) fields and high field strength in relation to input power level [1]. The statistical uniformity of the field allows a test object to be illuminated with a uniform (average) power level and is typically accomplished by varying the chamber boundary conditions with a rotating mechanical tuner (or paddle wheel).

A parameter that provides a considerable amount of insight with regard to the overall operation of a chamber is the power gain, as a function of frequency, between a transmitting antenna inside the chamber and a receiving antenna/sensor inside the chamber. First-order theoretical models for this parameter are derived in Sections II and III of this paper. The results of these idealized calculations are compared with corresponding experimental results in Section IV.

A block diagram of the chamber apparatus that has been developed for this study is shown in Fig. 1. The dimensions of the welded aluminum-alloy chamber are 1.034 m x 0.809 m x 0.581 m. This chamber, though small compared to others [2]–[4], is suitable for this particular study since it is not necessary to place large test objects inside. Chamber port 1 is the transmitting port; and port 2 is the receiving port, serving either a receiving antenna or a receiving D-dot sensor. Both the transmitting and receiving antennas are log-periodic dipole arrays. The D-dot sensor measures the time derivative of the electric displacement D and will be discussed in more detail in Section III. Using the receiving antenna is referred to as configuration 1; using the sensor, configuration 2. Additional details regarding the apparatus are given in Section IV.

II. Theoretical Gain of the Chamber with Receiving Antenna

A calculation for the power transfer characteristic, or gain, of the chamber in configuration 1 is presented in this section. This calculation can be initiated from the definition of the gain in (1).

Manuscript received June 9, 1995; revised December 15, 1995.

This work was supported by the National Aeronautics and Space Administration through Langley Research Center grant NAG-1-1510.

The authors are with the Department of Electrical Engineering, Texas Tech University, Lubbock, TX 79409 USA.

Publisher Item Identifier S 0018-9375(96)03858-6.

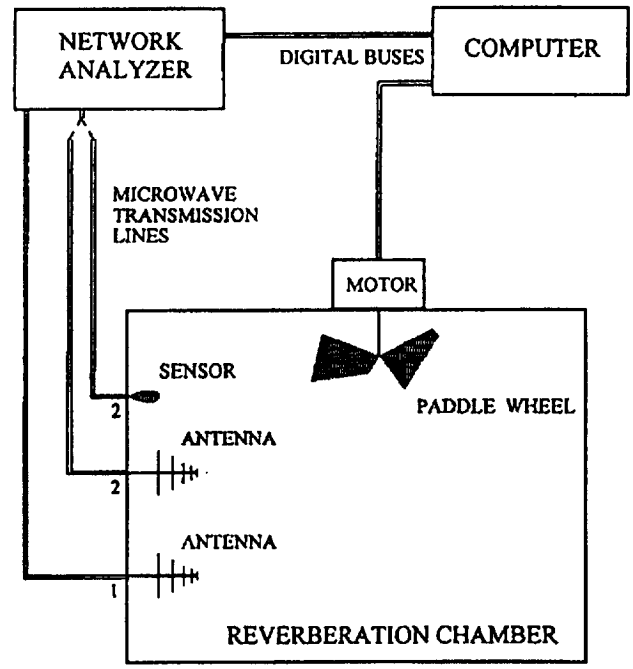

Fig. 1. Reverberation chamber system.

$$G_{\text{ant}} = \frac{P_d}{P_o} \tag{1}$$

where G_{ant} is the gain of the chamber with receiving antenna, P_o is the power delivered to the chamber from the transmitting antenna, and P_d is the power available to the receiving antenna from the chamber.

Next, (1) can be manipulated as follows:

$$G_{\text{ant}} = \frac{\omega W}{P_o} \Big/ \frac{\omega W}{P_d} = \frac{Q_{\text{net}}}{Q_{\text{ant}}} \tag{2}$$

where ω is the microwave radian frequency, W is the average energy stored in the chamber, Q_{net} is the overall Q of the chamber, and Q_{ant} is the contribution to the overall Q due to the receiving antenna.

Due to the parallel loading effect of the chamber walls and the antenna, the reciprocal of Q_{net} can be expressed by (3) [7].

$$\frac{1}{Q_{\text{net}}} = \frac{1}{Q_{\text{ant}}} + \frac{1}{Q_{\text{eqv}}} \tag{3}$$

where Q_{eqv} is the contribution to the overall Q due to the walls.

Substitution of (3) into (2) yields the following simplified expression for the gain.

$$G_{\text{ant}} = \frac{\left(\frac{1}{Q_{\text{ant}}} + \frac{1}{Q_{\text{eqv}}}\right)^{-1}}{Q_{\text{ant}}} = \frac{1}{1 + \frac{Q_{\text{ant}}}{Q_{\text{eqv}}}}. \tag{4}$$

An expression for Q_{eqv}, derived in [7], is given in (5).

$$Q_{\text{eqv}} = \omega \frac{W}{P_{\text{eqv}}} = \frac{3}{2} \frac{V}{\mu_r S \delta} \tag{5}$$

0018-9375/96$05.00 © 1996 IEEE

where P_{eqv} is the total power lost to the chamber walls, V is the volume of the chamber, μ_r is the relative permeability of the chamber walls, δ is the skin depth of the chamber walls, and S is the surface area of the chamber walls. This limiting case corresponds to the case of a highly "overmoded" cavity where the source wavelength is infinitesimally small in relation to the chamber dimensions and is an approximation that is frequently applied in the analysis of microwave reverberation chambers [4].

An expression for Q_{ant} can be derived from an expression for the average effective area of a receiving antenna with an incident signal that is randomly polarized [9]. This expression is given by (6).

$$\overline{A} = \frac{\lambda^2 \overline{D}}{8\pi} \tag{6}$$

where $\overline{A}$ is the average effective area, λ is the microwave wavelength, and $\overline{D}$ is the average directivity of the antenna. Ideally, the average directivity of a antenna in a microwave reverberation chamber is unity [7] since a high degree of statistical homogeneity of the field can be assumed when the chamber size is (ideally) much larger than the microwave source wavelength. With this assumption, the average power delivered to the antenna, P_d, can be calculated as follows:

$$P_d = \left(\frac{\lambda^2}{8\pi}\right)\left(\frac{Wc}{V}\right) \tag{7}$$

where c is the speed of light. Here, the quantity in the second parenthesis is the average power density in the chamber. This equation (7) can be manipulated to yield an expression for Q_{ant}

$$Q_{ant} = \frac{\omega W}{P_d} = 2\left(\frac{\omega}{c}\right)^3 \frac{V}{\pi} \tag{8}$$

where the relation $\lambda = 2\pi c/\omega$ has been used.

Substitution of the above expressions for Q_{ant} and Q_{eqv} (8) and (5) into (4) yields the desired expression for the gain of the chamber in configuration 1

$$G_{ant} = \frac{1}{1 + \frac{4}{3}\sqrt{\frac{2\mu_r}{\mu_0 \sigma}} \frac{S}{c^3 \pi} \omega^{2.5}} \tag{9}$$

where the relations $\delta = \sqrt{2/\omega\mu\sigma}$ and $\mu = \mu_o \mu_r$ have been applied, with μ_o the permeability of free space and σ the conductivity of the chamber walls.

III. Theoretical Gain of the Chamber with Receiving D-Dot Sensor

A calculation for the gain of the chamber in configuration 2 can be performed in the same manner as the gain calculation in Section II. The initial steps are identical, and (4) is modified as follows:

$$G_{\dot{D}} = \frac{1}{1 + \frac{Q_{\dot{D}}}{Q_{eqv}}} \tag{10}$$

where $G_{\dot{D}}$ is the gain of the chamber with receiving D-dot sensor and $Q_{\dot{D}}$ is the contribution to the overall Q due to the receiving D-dot sensor. Here, Q_{eqv} is given by (5).

An expression for $Q_{\dot{D}}$ can be derived from a first-order model for the operation of a D-dot sensor. This model [10] relates the voltage at the sensor output terminals to the electric field at the chamber wall as follows:

$$\overline{v}_{\dot{D}} = RA\varepsilon_0 \omega \overline{E}_n \tag{11}$$

where $\overline{v}_{\dot{D}}$ is the average of the magnitude of the sensor output voltage, $\overline{E}_n$ is the average of the magnitude of the normal electric field at the chamber wall, R is the sensor load resistance, A is the sensor equivalent area, and ε_0 is the permittivity of free space. Also, a relationship between the average normal field magnitude at a chamber wall and the average energy density in the chamber is derived in [5] and is presented here as (12)

$$\varepsilon_0 \overline{E}_n^2 = \frac{2U}{3} \tag{12}$$

where U is the average energy density in the chamber. These two expressions (11) and (12) can be combined to obtain the following relationship for $Q_{\dot{D}}$

$$Q_{\dot{D}} = \frac{\omega W}{P_d} = \frac{\omega U V R}{\overline{v}_{\dot{D}}^2} = \frac{3}{2}\frac{V}{RA^2 \varepsilon_0 \omega}. \tag{13}$$

This equation, along with (5), can now be substituted into (10) to obtain the desired equation for the gain of the chamber in configuration 2

$$G_{\dot{D}} = \frac{1}{1 + \sqrt{\frac{2\mu_r}{\mu_0 \sigma}} \frac{S}{RA^2 \varepsilon_0} \omega^{-1.5}} \tag{14}$$

where the relations $\delta = \sqrt{2/\omega\mu\sigma}$ and $\mu = \mu_0 \mu_r$ have been applied.

IV. Comparison of Theoretical Models to Measured Response

The apparatus shown schematically in Fig. 1 was used to measure chamber gain for comparison with the theoretical models of (9) and (14). The network analyzer (Hewlett Packard 8719A, 130 MHz to 13.5 GHz) serves as microwave source and receiver and measures the S-parameters, $S_{11}, S_{22}, S_{12}, S_{21}$, of the chamber. During the measurements the analyzer is controlled by the computer (486 PC), as is the paddle wheel motor (60 oz-in stepper motor with 10 : 1 planetary gearhead). Located inside the chamber are the antennas, sensor, and paddle wheel. The antennas are linearly polarized log-periodic dipole arrays (Watkins-Johnson WJ-48195, 1.0 to 18.0 GHz) and are mounted well apart and with perpendicular polarizations in order to minimize direct coupling between them. The sensor is a surface-mounted asymptotic conical dipole D-dot sensor [10] (Prodyn Technologies AD-S10(R), $A = 1.0 \cdot 10^{-4}$ m^2, 3-dB point = 10 GHz) and is mounted to a chamber wall where the electric field is perpendicular to the polarization of the transmitting antenna to minimize coupling. The sensor is used at frequencies up to its 3 dB point, where its response has fallen to 3 dB below the first-order model of (11), by correcting the sensor output values for this falloff during data analysis. The paddle wheel has four dissimilar, obliquely bent aluminum blades which measure 0.700 m from tip to opposite tip. Access to the chamber interior is achieved by removing a bolted-on, gasketed panel.

Plots of measured chamber gain for configuration 1 and configuration 2 are shown in Figs. 2 and 3, respectively. The corresponding theoretical models are also plotted in these figures, (9) in Fig. 2 and (14) in Fig. 3. The measurements presented in these figures were conducted with a 21 point frequency sweep from 1 to 10 GHz. A total of 153 separate gain measurements were accumulated for each frequency point. Each of these measurements was taken with the paddle wheel adjusted to a unique angular position controlled by the stepper motor, which was programmed to turn the paddle wheel one complete revolution in 153 equal angular increments.

The gain values in Figs. 2 and 3 were obtained from S_{21} and S_{11} measurements as follows:

$$G_{21} = \frac{|S_{21}|^2}{1 - |S_{11}|^2} \tag{15}$$

where G_{21} is the measured power gain from the transmitting port (port 1 in Fig. 1) to the receiving port (port 2 in Fig. 1), $|S_{21}|$ is the

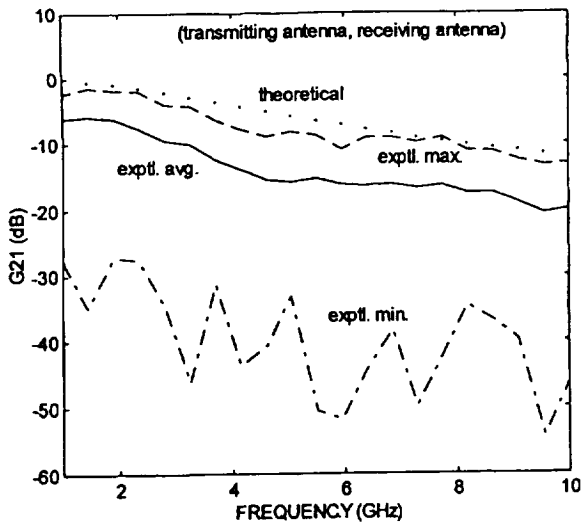

Fig. 2. Chamber gain versus frequency in configuration 1.

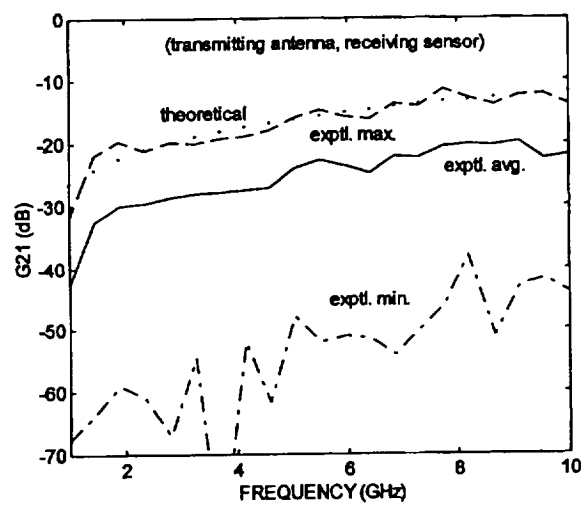

Fig. 3. Chamber gain versus frequency in configuration 2.

magnitude of the voltage transmission coefficient from port 1 to port 2, and $|S_{11}|$ is the magnitude of the voltage reflection coefficient at port 1. The $1 - |S_{11}|^2$ term is included to account for power returned to the source from the transmitting antenna. An important characteristic of the experimental curves in both Figs. 2 and 3 is the large, greater than 20 dB, difference between the maximum and minimum values of G_{21} over the entire frequency interval. This large difference is generally desirable with regard to proper reverberation chamber operation and is an indication of a properly functioning paddle wheel.

As might be expected, the theoretical curves in both Figs. 2 and 3 are only approximate representations of the actual response of the chamber. The slopes of the theoretical curves match the general trends of the slopes of the experimental maximum and average curves, but the theoretical values tend to be larger than the experimental. This discrepancy can perhaps be attributed to factors such as losses in the paddle wheel blades, antenna internal and mismatch losses, and losses through the access panel gasket, which were not modeled and included in the calculations. Regarding chamber wall losses, which were modeled, the value used for the wall conductivity, σ, was $2.32 \cdot 10^7$ S/m. Although this is the handbook value [11] for our particular aluminum alloy (6061T6), it may in fact be too high [8]; and this would add to the discrepancy.

Some insight into the physical phenomena that determine the shape of the chamber response can be obtained from an examination of equations used in the models. For example, for configuration 1 the $\omega^{2.5}$ dependence in the second term of the denominator of (9) can be attributed to the loading of the receiving antenna decreasing with ω^2 combined with the chamber wall loss increasing with $\omega^{1/2}$. Specifically, the ratio of Q's in (4) can be rewritten as a power ratio as follows:

$$\frac{Q_{\text{ant}}}{Q_{\text{eqv}}} = \frac{\omega W}{P_d} \Big/ \frac{\omega W}{P_{\text{eqv}}} = \frac{P_{\text{eqv}}}{P_d}. \tag{16}$$

Here, $P_d \propto \omega^{-2}$ from (7) and $P_{\text{eqv}} \propto \omega^{1/2}$ from (5) since $\delta \propto \omega^{-1/2}$.

At low frequencies, however, the first term in the denominator of (9) dominates. Thus, there are two distinct frequency regions. The transition point between these two regions can be calculated by setting the second term in the denominator equal to unity and solving for the corresponding value of ω. The result is a transition point for our chamber at 3.34 GHz. Below this transition point, $P_d > P_{\text{eqv}}$ in (16), so that power extraction from the chamber by the receiving antenna dominates over power loss to the chamber walls.

Similarly, for configuration 2 the $\omega^{-3/2}$ dependence in the second term of the denominator of (14) is due to the ω^2 variation in the D-dot sensor loading combined with the $\omega^{1/2}$ variation in the chamber wall loss. (The frequency dependence of the sensor loading can be observed by solving for P_d in (13).)

The first term of the denominator of (14) becomes important only for high frequencies—well above 10 GHz for our particular chamber and sensor. This is the range where the power extracted by the sensor is dominant. Over the interval of our measurements, 1–10 GHz, the chamber wall loss dominates.

References

[1] D. A. Hill, "Electronic mode stirring for reverberation chambers," *IEEE Trans. Electromag. Compat.*, vol. 36, pp. 294–299, Nov. 1994.

[2] B. H. Liu and D. C. Chang, "Eigenmodes and the composite quality factor of a reverberating chamber," NBS Tech. Note 1066, Aug. 1983.

[3] M. L. Crawford and G. H. Koepke, "Design, evaluation, and use of a reverberation chamber for performing electromagnetic susceptibility/vulnerability measurements," NBS Tech. Note 1092, Apr. 1986.

[4] J. G. Kostas and B. Boverie, "Statistical model for a mode-stirred chamber," *IEEE Trans. Electromag. Compat.*, vol. 33, pp. 366–370, Nov. 1991.

[5] J. M. Dunn, "Local, high-frequency analysis of the fields in a mode-stirred chamber," *IEEE Trans. Electromag. Compat.*, vol. 32, pp. 53–58, Feb. 1990.

[6] T. F. Trost, A. K. Mitra, and A. M. Alvarado, "Characterization of a small microwave reverberation chamber," in *Proc. 11th Int. Zurich Symp. Tech. Exh. Electromag. Compat.*, 1995, pp. 583–586.

[7] T. A. Loughry, "Frequency stirring: An alternate approach to mechanical mode-stirring for the conduct of electromagnetic susceptibility testing," Phillips Laboratory Tech. Report 91-1036, Nov. 1991.

[8] D. A. Hill *et al.*, "Aperture excitation of electrically large, lossy cavities," *IEEE Trans. Electromag. Compat.*, vol. 36, pp. 169–178, Aug. 1994 .

[9] C. T. Tai, "On the definition of the effective aperture of antennas," *IEEE Trans. Antennas Propagat.*, vol. 9, pp. 224–225, Mar. 1961.

[10] C. E. Baum *et al.*, "Sensors for electromagnetic pulse measurements both inside and away from nuclear source regions," *IEEE Trans. Electromag. Compat.*, vol. 20, pp. 22–35, Feb. 1978.

[11] J. H. Potter, *Handbook of the Engineering Sciences*, vol. II. Princeton, NJ: Van Nostrand, 1967, p. 858.